Static performance of square CFDST chord to steel SHS brace T-joints

You-Fu Yang[1,*]; Xue-Meng Bie[1]; Feng Fu[2]

[1] *State Key Laboratory of Coastal and Offshore Engineering, Dalian University of Technology, Dalian, 116024, China*
[2] *Department of Civil Engineering, School of Mathematics, Computer Science & Engineering, City University London, Northampton Square, London, UK*

Abstract: In this paper, static performance of square concrete-filled double-skin steel tube (CFDST) chord to steel square hollow section (SHS) brace T-joints are investigated through experimental and numerical studies. Twelve specimens, including 8 T-joints with square CFDST chord, 2 T-joints with square concrete-filled steel tube (CFST) chord and 2 T-joints with steel SHS chord as counterparts, were tested under continuously increasing compressive force on the brace with concentric compression load applied simultaneously to the chord. The influence of chord type, brace-to-chord width ratio (β) and concentric compression level of the chord (n) on the static performance of the T-joints was examined. It is found that the composite T-joints have enhanced static performance than their steel counterparts. For the composite T-joints, the failure pattern varies from compression-flexure-shear failure of composite chord to local buckling of steel SHS brace when β reduces. Moreover, while only the composite chord failure occurs, the bearing capacity of the specimens augments with growing of hollow ratio of CFDST chord (χ), β and n; however, when only steel SHS brace of the composite joints fails, the chord type has a moderate influence on the bearing capacity of the specimens. The static performance of the T-joints was simulated using a finite element (FE) model, which is validated against the observations in the experiment. On the basis of the experimental and numerical research, the design formulae for bearing capacity of the composite T-joints were developed, and a good accuracy of the computations was achieved.

Key words: T-joint; square hollow section (SHS); concrete-filled double-skin steel tube (CFDST); static tests; finite element simulation; bearing capacity computation

*Corresponding author. Tel.: 86-411-8470 8510; Fax: 86-411-8467 4141.
E–mail address: youfuyang@163.com (Dr. You-Fu Yang).

1. Introduction

Due to the excellent structural performance and attractive aesthetic effect, steel hollow section trussed structures are adopted extensively in buildings, bridges, offshore structures, towers and masts, and so on [1], in which the joints are subjected to the most complicated loadings, causing complicated interaction between chords and braces. Generally, the chords and braces in a steel hollow section truss are connected through welding; however, the welded joints may prone to fail due to their low strength and poor fatigue resistance caused by the severe concentration of stress in welding zone as well as the existence of the initial defects of welding. To improve the structural performance of the welded joints between steel hollow section chords and braces, Packer [2] first proposed a new kind of composite tubular joints with the chord fully or partially filled with concrete, i.e. steel hollow section brace(s) to concrete-filled steel tube (CFST) chord joints. However, when the outer size of the chord is increased, the filling concrete will restrict the practical application of the composite tubular joints owing to the increased weight of the structure and the labor cost. In such a case, replacing CFST with the novel concrete-filled double-skin steel tube (CFDST) becomes a good choice. Generally, CFDST, which is composed of two concentric steel tubes and concrete between them, is a sort of new composite member originated from the CFST, and through reasonable design the composite tubular joints with CFDST chords can be lighter than those with CFST chords while maintaining the similar performance [3-5]. Typical on-sight photo and schematic view of composite tubular joints are demonstrated in Fig. 1.

The earliest research towards the static property of the composite T- and K-joints using rectangular CFST chord and steel hollow section brace was reported by Packer [2], where three tension-loaded T-joints and six gapped K-joints were tested and the results indicated that the composite tubular joints had a significant different failure pattern and a superior strength relative to their counterparts with steel hollow section chord and brace(s). Since then, some researchers started to pay attention to the structural or fatigue behaviour of the composite tubular joints, including experimental investigation into circular CFST chord to steel circular hollow section (CHS) brace T-joints subjected to uniplanar monotonic and cyclic bending at the brace end with axial compression applied to the chord [6,7] and cyclic axial loading upon the brace [8], CFST T- and X-joints manufactured from stainless steel square hollow section (SHS) and rectangular hollow section (RHS) subjected to concentric compression at one brace end [9, 10], square CFDST chord to steel SHS brace X-joints under axial compression upon braces [11], circular CFDST chord to steel CHS brace(s) T- and K-joints under static loading [12, 13], full-scale K-joints adopting steel CHS brace and circular CFST chord under static loading [14], square CFST chord to steel SHS brace T-joints subjected to uniplanar fatigue loading upon the brace [15], circular CFST chord to steel CHS brace X-joints with axial loading applied to the chord [16], unreinforced and reinforced circular CFST chord to steel CHS brace K-joints with axial tensile load upon the chord [17-19], and T-, Y-, K-, and KT-joints using steel CHS brace and circular CFST chord with axial tensile load upon one brace [20, 21], and numerical simulation of T- and K-joints using steel CHS brace and circular CFDST chord under static loading [12, 22], steel CHS braces to circular CFST chord N-joints with axial loading applied to the brace end [23], circular CFST chord to steel CHS brace T-joints with axial loading acting on the brace end [24, 25], unreinforced and reinforced circular CFST chord to CHS steel brace K-joints with axial tensile load upon the chord [18, 19], and T-, Y-, K-, and KT-joints using steel CHS brace and circular CFST chord with axial tensile load upon one brace [26]. Furthermore, the simplified formulae for the static strength of K-joints using steel CHS brace and circular CFDST chord [22], the stress concentration factors (SCFs) of T- and N-joints using circular CFST chord and steel CHS brace with axial loading applied to the end of the braces [23, 25], and the ultimate strength of circular CFST chord to steel CHS brace T- and Y-joints with chord broken by punching and shearing [26], have also been recommended. Previous studies have revealed that: 1) compared to the corresponding steel tubular joints the composite tubular joints possess different failure patterns and higher strength and stiffness, 2) filling concrete into the chord greatly enhances the seismic performance of the steel hollow section joints, 3) the welded composite tubular joints generally have lower peak SCFs and better fatigue strength than the steel counterparts, and 4) the existing design method for the steel tubular joints cannot be directly applied to the design of composite joints.

It is also noticeable that, only few researchers [2, 9-11, 15] carried out the study on the static or fatigue performance of the composite T-, K- and X-joints using square/rectangular CFST/CFDST chord, and developped the static strength calculation formulae or fatigue design method of such kind of joints. These studies provide the basis for the research of the composite T-joints having square CFDST chord with pined-pined ends. Therefore, this paper tries to experimentally and numerically investigate the behaviour of square CFDST chord to steel SHS brace T-joints under static loading. The design formulae for the bearing capacity of such composite joints were eventually put forward according to the results of systematic finite element simulation.

2. Experimental investigation

2.1. Material properties

Standard tensile coupon tests were performed to measure the properties of steel, and the results are given in Table 1. According to EC3 [27] and ANSI/AISC-360 [28], the SHS with width and thickness of 200 mm and 4.00 mm belongs respectively to the Class 4 and non-compact section, i.e. local buckling will occur before achieving its yield strength in one or more parts of the cross-section, whilst other steel SHSs belong to the compact section. Furthermore, according to [5], the SHS with width and thickness of 200 mm and 4.00 mm will not buckle in advance due to the supporting effect of the sandwiched concrete when it is used as the outer tube of CFDST.

Concrete mix with design strength class C45 was poured into the sandwich between two tubes or the outer tube of the composite chords. The mix-proportion of the concrete was as follows: P.O42.5 cement, 420 kg/m^3; the first grade fly ash, 130 kg/m^3; limestone rubble with particle size of 5-10 mm, 832 kg/m^3; river sand, 800 kg/m^3; tap water, 189.5 kg/m^3; and Polycarboxylate water reducing agent, 6.88 kg/m^3. The fresh concrete had a slump of 270 mm and a spreading of 661 mm. To measure the compressive strength and modulus of elasticity of the concrete, a number of cubes with 150 mm side length and prisms with dimensions of 150 mm×150 mm×300 mm were fabricated using standardized molds and maintained under standard curing conditions. The compressive strength of the concrete was 52.4 MPa and 80.2 MPa respectively at the time of 28 days and T-joint experiment, and the modulus of elasticity of the concrete was 34,700 N/mm^2.

2.2. Test specimens

A total of 12 specimens, including 8 T-joints using square CFDST chord, 2 T-joints using square CFST chord and 2 T-joints using steel SHS chord as counterparts, were tested under monotonically varied compressive force upon the top of steel SHS brace with the chord concentrically restrained.

The parameters used in the experiment are as follows:

- Chord type: square CFDST with hollow ratio (χ) of 0.3 and 0.5, square CFST and steel SHS;
- Brace-to-chord width ratio (β): 0.3 and 0.5; and
- Concentric compression level of the chord (n): 0.04~0.4.

The hollow ratio of CFDST chord (χ), brace-to-chord width ratio (β) and concentric compression level of the chord (n) of the tested specimens are defined as follows,

$$\chi = b_\mathrm{i}/(b_\mathrm{o} - 2t_\mathrm{o}) \tag{1}$$

$$\beta = b_\mathrm{b}/b_\mathrm{o} \tag{2}$$

$$n = N_0/N_\mathrm{cr} \tag{3}$$

where, N_0 is a constant concentric compressive load applied to the chord of the T-joints throughout the whole process of testing; and N_cr is the axial capacity of individual composite and steel chords, which is calculated using the simplified formulae in [29] and [27], respectively.

The specimens are the scaled-down from the actual structural T-joints. The dimensions of the tested specimens are determined by referring to the previous studies [2, 9-11, 15], and further considering the limitations of the test site and the capacity of the equipment. The important factors affecting the static behaviour of the composite T-joints contain material, geometric and load parameters. The selected steel SHSs with different properties, hollow ratio of CFDST chord (χ), brace-to-chord width ratio (β) reflect the material and geometric parameters; whilst the selected concentric compression level of the chord (n) reflects the load parameters. The variation range of the parameters is generally controlled to represent the T-joint configuration and design method in practice.

The configurations of the specimens are illustrated in Fig. 2, where b_o (b_i) and t_o (t_i) are the overall width and wall thickness of outer (inner) steel SHS in the chord respectively, b_b and t_b represent the overall width and the corresponding wall thickness of steel SHS brace, respectively, w is the weld size, and the remaining dimensions are in mm. The length of the brace and chord in all specimens is the same, which equals to 400 mm and 1,200 mm, respectively. Table 2 summarizes the detailed information of the specimens, where $F_{ue,j}$ is the measured bearing capacity; $\Delta_{mc,ue}$ and $\Delta_{tb,ue}$ are the vertical displacement at the chord mid-span and the brace top while achieving $F_{ue,j}$, respectively; and $F_{ufe,j}$ is the simulated bearing capacity based on the finite element (FE) model. Regarding the labels in Table 2, the composite chord and steel SHS chord is respectively denoted by the capital letters 'C' and 'S' in the first part, and χ of the chord in the composite T-joints follows the capital letter 'C', whilst β and n are demonstrated in the second and third parts, respectively.

Outer and inner SHS of the chords and the SHS braces were all fabricated using cold-formed square steel tubes. The length of each steel SHS was determined by its length in different T-joint specimens, and the ends of each steel SHS was further treated as flat before welding. Fillet welds with shielded metal-arc welding were used to weld the brace and the outer tube of the chord, and the weld sizes (w, as shown in Fig. 2) of the specimens were all greater than $1.5t_b$. The 2.5 mm, 3.2 mm and 4.0 mm electrodes with nominal 0.2% proof stress, tensile strength and elongation of 400 MPa, 480 MPa, and 22%, respectively, were used for welding. The quality of all welds was strictly controlled to meet the requirements of effective force transfer. At the same time, each chord had two square steel endplates of 280 mm side length and 20 mm thickness, and each brace had one square steel endplate of 180 mm side length and 20 mm thickness, as shown in Fig. 2.

2.3. Test rig and measuring instruments

A set of test rig for the T-joints was specially designed, as shown in Fig. 3. One end of the horizontally placed chord is concentrically restrained through a one-way plate hinge bolted to a fixed reaction block, whilst the other end is connected to a solid rod capable of moving horizontally. A 2,000 kN hydraulic jack connecting the solid rod and a fixed reaction block was adopted to apply the constant concentric compressive load (N_0), and a 2,000 kN servo actuator connected to the top of brace by a rigid component was selected to apply the varied compressive force. Moreover, in order to ensure that the whole T-joint specimen moved in the vertical plane, the possible out-of-plane deformation in the joint was prevented by two pairs of lateral bracings on both sides of the chord. At the same time, four bearings were arranged along the height direction of each lateral bracing to eliminate the friction resistance of the chord wall, hence during the movement of the chord there were always two bearings in contact with its side walls.

Each T-joint specimen was fitted with 4 displacement transducers, among which three were used to record vertical displacements of key position of the chord and one was used to monitor vertical displacements at the top of the brace. Furthermore, to examine the representative strain development of the outer SHS in the chord and the SHS brace, strain gauges were longitudinally and transversely installed at the mid-span section of the steel tube outside the chord and longitudinally pasted at the half-height section of the brace, and a total of 14 strain gauges were arranged for each specimen, as shown in Fig. 3. The forces on the top of the brace and the representative deformations of the chord and brace were acquired by a data logger.

The displacement control loading method with a loading rate of 0.5 mm/min was adopted in the current tests. The test was terminated when any of the following three conditions were achieved: 1) the vertical displacement of the chord mid-span section was larger than 1/20 of the chord effective span, 2) the load resistance decreased to about 60% of the measured peak force, or 3) the obvious downward displacements of upper flange of the chord were produced at the joint zone.

3. Experimental results and discussion

3.1. Loading process and failure patterns

Detailed observation of the experimental process showed that there was no significant change in the welds, i.e. the quality of the welds could guarantee that the failure of the specimen occurred only in the chord or brace. The loading process of the T-joints with composite chord was obviously different from those using steel SHS chord. For the steel T-joints, the concavity damage at the joint zone started from the upper flange of steel SHS chord as well as the bulge appeared at the webs next to the upper flange increased quickly with increase of the vertical forces until failure happened, and throughout the loading process the vertical displacements at the lower surface of the chord were limited and there was no sign of destruction for the brace, considering that the chord in the steel T-joints pertained to the non-compact steel section [27, 28]. For the composite T-joints with β of 0.3, the interval bulge damage started at one end or both ends of the brace became more and more obvious with increase of the forces until failure, and the vertical displacements at the lower surface of the composite chord were also limited. For the composite T-joints with β of 0.5, either on one side or both sides of the brace the local buckling of the top flange of the outer chord tube occurred first and then extended to both webs of the outer chord tube until failure, and the vertical displacements at the lower surface of the chord continued to increase with increase of the forces.

Fig. 4 demonstrates the final failure pattern of all specimens. It is shown that, for the composite T-joints with β of 0.5, local buckling is observed at upper flange and partial webs close to the upper flange of the outer SHS in the chord; however, there is no obvious damage to the steel SHS brace. The difference of buckling position and number of outer tube of the chord may be caused by the random distribution of initial material defects. For the composite T-joints with β of 0.3, local buckling at both ends and overall in-plane lateral deformation of steel SHS brace happen and there is no obvious destruction in the composite chord. However, for the steel T-joints, flange yielding and web buckling of steel SHS chord are observed under the concentrated loading from the steel SHS brace [27, 28], and there is no obvious damage to the brace.

It was observed from the tests that there were three types of failure pattern for the concrete in the composite chord, as indicated in Fig. 5. As can be found in Figs. 5(a) and 5(b), for the chords having local buckling in outer steel SHS, crushing of concrete was observed at the buckling positions together with cracking of concrete in the tension area, and there is a square ring indentation on the upper surface of the concrete. However, for the chords having local buckling in steel SHS brace, there is no obvious damage to the concrete (Fig. 5(c)).

Similar to the concrete, the inner steel SHS in the square CFDST chords mainly exhibited three kinds of failure patterns, as demonstrated in Fig. 6. As can be observed in Fig. 6(a), for the chords with $\chi = 0.5$ and $\beta = 0.5$, the combined inward local buckling as well as overall deflection occur to the inner steel SHS under the lateral loading and concentric compression due to the decreased local stability with a larger $b_{\mathrm{i}}/t_{\mathrm{i}}$, and the inward local buckling becomes more serious with increase of n. As can be seen in Fig. 6(b), for the chords with $\chi = 0.3$ and $\beta = 0.5$, only the overall deflection of the inner steel SHS is produced irrespective of n value, as the stability of the inner steel SHS with a smaller $b_{\mathrm{i}}/t_{\mathrm{i}}$ becomes better. It is shown in Fig. 6(c) that, for the composite T-joints with only brace destruction ($\beta = 0.3$), the inner steel SHS has no evident damage.

The failure patterns of the T-joint specimens observed in the experiments are also summarized in Table 2.

3.2. Force-displacement curves

The recorded force (F) versus vertical displacement (Δ_{tb} and Δ_{mc}) relationship of the composite and steel T-joints are illustrated in Fig. 7, where F is the recorded forces on the top of the steel SHS brace, and Δ_{mc} and Δ_{tb} are the measured vertical displacements at the chord mid-span and at the brace top, respectively. The measured bearing capacity (F_{ue}) and the vertical displacements corresponding to F_{ue} ($\Delta_{\mathrm{mc,ue}}$ and $\Delta_{\mathrm{tb,ue}}$) of all T-joints are presented in Table 2. The recorded peak force and the corresponding vertical displacements of the composite T-joints are defined as F_{ue} and $\Delta_{\mathrm{mc,ue}}$ ($\Delta_{\mathrm{tb,ue}}$), respectively. For the reference steel T-joints, the ultimate deformation limit criterion proposed in [30] is employed to determine the bearing capacity. The 1.5 times of force corresponding to the deformation of the upper flange of the steel SHS chord (δ_{f}) reaching 1%b_{o} is defined as F_{ue}, and the corresponding vertical displacements in $F - \Delta_{\mathrm{tb}}(\Delta_{\mathrm{mc}})$ curves is thus regarded as $\Delta_{\mathrm{mc,ue}}$ ($\Delta_{\mathrm{tb,ue}}$). The following formulae are adopted to compute δ_{f}:

$$\delta_{\mathrm{f}} = \Delta_{\mathrm{tb}} - \Delta_{\mathrm{mc}} - \delta_{\mathrm{b}} \tag{4-1}$$

$$\delta_{\mathrm{b}} = \frac{F \cdot l_{\mathrm{b}}}{A_{\mathrm{b}} \cdot E_{\mathrm{bs}}} \tag{4-2}$$

where, δ_{b} is the compression deformation of steel SHS brace, and E_{bs}, A_{b} and l_{b} are the modulus of elasticity, cross-sectional area and length of steel SHS brace, respectively.

As can be detected from Fig. 7 that, for all specimens Δ_{tb} are always greater than Δ_{mc} during the loading process due to the compression deformation of steel SHS brace as well as the partial chord beneath it. As can be found in Figs. 7(a) and 7(b), when $\beta = 0.5$, the composite T-joints having a bigger n possess a larger initial slope of $F - \Delta_{\mathrm{tb}}(\Delta_{\mathrm{mc}})$ curves and descending slope of $F - \Delta_{\mathrm{tb}}(\Delta_{\mathrm{mc}})$ curves after achieving F_{ue}, and χ also has an obvious influence on the descending slope of $F - \Delta_{\mathrm{tb}}(\Delta_{\mathrm{mc}})$ curves. This is probably because the increased constraint induced by the increase of n improves the lateral resistant stiffness of the chord, resulting in a larger initial slope; however, the increase of concentric compression load leads to the increased second-order effect, which produces a quicker decrease of load after achieving F_{ue}. Moreover, after reaching F_{ue}, the inner tube of square CFDST chord in the composite T-joints having a larger χ is apt to buckle owing to a larger $b_{\mathrm{i}}/t_{\mathrm{i}}$ and thus reducing the support effect of the sandwiched concrete and inner tube to the outer tube. It is shown in Figs. 7(c) and 7(d) that, the effect of χ on the initial and falling slope of $F - \Delta_{\mathrm{tb}}(\Delta_{\mathrm{mc}})$ curves of the composite T-joints having $\beta = 0.3$ as well as $n = 0.2$ is moderate; however, Δ_{mc} quickly decreases after reaching F_{ue} as the failure only occurs to the brace. Under the same β and n values, the composite T-joints have a larger initial slope of $F - \Delta_{\mathrm{tb}}(\Delta_{\mathrm{mc}})$ curves and descending slope of $F - \Delta_{\mathrm{tb}}(\Delta_{\mathrm{mc}})$ curves after achieving F_{ue} than the corresponding steel T-joint, because of the contribution of the inner tube as well as the sandwiched concrete before achieving F_{ue}, and the inner tube local buckling and/or the sandwiched concrete crushing after reaching F_{ue}.

It was observed that there were three types of vertical displacement patterns along the effective span of the chord, as typically shown in Fig. 8, where u_{c} is the recorded vertical displacements by three displacement transducers on the chord, L_{ce} is the effective span of the chord (1430 mm) between two hinge supports, y is the distance from one hinge support, and $f(= F/F_{\mathrm{ue}})$ is the force ratio and positive and negative values represent the load rising stage before F_{ue} and the load falling stage after F_{ue}, respectively. It is shown that, for the T-joints having chord destruction (e.g. C0.5-0.5-0.2 or S-0.3-0.2), u_{c} continually increase with the variation of f till the end of the tests as the brace without reaching the bearing capacity can always transmit vertical forces to the chord, and the distribution of vertical displacements is generally symmetric about the mid-span of the chord; however, u_{c} of steel T-joints are obviously lower than those of the composite counterparts, as the chord destruction in the steel T-joints mainly appeared in the limited zone of the upper flange of the steel SHS chord. Moreover, for the composite T-joints having brace destruction (e.g. C0.5-0.3-0.2), u_{c} increase with increase of f before reaching F_{ue} under the vertical forces transmitted by the brace, and after that u_{c} decrease with decrease of f due to the elastic recovery of the displacements of the chord without reaching the bearing capacity, and the distribution of vertical displacements is not symmetric about the mid-span of the chord.

3.3. Strain development

Fig. 9 demonstrates the force (F) versus strain (ε) relationship in the chord of typical specimens at different measuring points, where $\varepsilon_{\mathrm{yo}}$ is the yield strain of outer chord tube. As can be observed, in general, the farther the measuring point is from the horizontal centroid axis (e.g. points a, b and d at the corner and point e at the center of lower flange) the faster the strain develops, and the strain development at the horizontal centroid axis (point c) are the slowest regardless of the type of the chord. Meanwhile, the variation of the strains at the upper and lower flange corners is opposite due to the action of moment produced by the lateral and concentric loads. For the composite T-joints having chord failure (see Figs. 9(a) and 9(b)), the longitudinal strain corresponding to F_{ue} at all measuring points is larger than $\varepsilon_{\mathrm{yo}}$, which indicates that the property of outer steel SHS can be fully utilized. However, for the composite T-joints having brace destruction, the strain at each measuring point changes substantially within the elastic range. Moreover, for the steel T-joints (see Fig. 9(c)), when achieving peak force the longitudinal strain at all measuring points has significant difference, i.e. values at the upper part (points a and b on the corner and point c at the horizontal centroid axis) are larger than $\varepsilon_{\mathrm{yo}}$, whilst values at the lower corner and flange (points d and e) are much smaller than $\varepsilon_{\mathrm{yo}}$ as the destruction is concentrated in the upper half of the steel SHS chord (see Fig. 4 (d)).

Fig. 10 illustrates the longitudinal strain (ε_{L}) distribution of the chords under different force ratio

(f). It is shown that, ε_{L} at the selected points of the chord of all specimens increases with increase of (f) before reaching F_{ue}. For the T-joint specimens with the composite chord, ε_{L} is generally linear along the height of the section, i.e. ε_{L} at the centroid axis (point c) is always smaller than $\varepsilon_{\mathrm{yo}}$ and varies within a limited range, and simultaneously, the farther away from the centroid axis, the more sufficient the longitudinal strain development, and ε_{L} at point a(b) and e(d) is larger than $\varepsilon_{\mathrm{yo}}$ when $n \geq 0.8$. The concentric compression level of the chord (n) mainly affects the initial strain of the chords has a moderate effect on the distribution characteristics of ε_{L}, whilst, under the same f value, the ε_{L} distribution of CFDST chords is similar to that of CFST chords, which indicates that the CFDST chord have similar performance to the corresponding CFST chord due to the presence of the inner tube. Moreover, compared with the composite chords, all ε_{L} of steel SHS chords are smaller than $\varepsilon_{\mathrm{yo}}$ and the maximum ε_{L} appear at point c due to the web buckling of the side walls near the point c.

Fig. 11 shows the impact of parameters on $f-\varepsilon_{\mathrm{L}}$ curve of the steel SHS brace, where ε_{L} is the average longitudinal strain recorded by four strain gauges, and $\varepsilon_{\mathrm{yb,100}}$ and $\varepsilon_{\mathrm{yb,60}}$ are the yield strain of the steel SHS brace with b_{b} of 100 mm and 60 mm, respectively. It is shown that, generally, a lower initial slope of $f-\varepsilon_{\mathrm{L}}$ relationship and a higher longitudinal strain corresponding to F_{ue} ($\varepsilon_{\mathrm{ue}}$) are produced, with increase of χ and n and decrease of β regardless of the chord type. This is mainly attributed to the fact that, the chord flexural stiffness is affected by three experimental parameters. Generally, $\varepsilon_{\mathrm{ue}}$ of the composite T-joints having $\beta = 0.3$ is larger than $\varepsilon_{\mathrm{by,60}}$ (see Fig. 11(b)) as the failure of specimens is governed by the steel SHS brace. $\varepsilon_{\mathrm{ue}}$ of three composite T-joints with $\beta = 0.5$ (i.e. C0.3-0.5-0.4, C0.5-0.5-0.2 and C0.5-0.5-0.4) is also larger than $\varepsilon_{\mathrm{by,100}}$ (see Fig. 11(a)) as their F_{ue} is higher than other specimens with $\beta = 0.5$, which have a smaller $\varepsilon_{\mathrm{ue}}$ than $\varepsilon_{\mathrm{by,100}}$. In addition, $\varepsilon_{\mathrm{ue}}$ of the steel T-joints is much smaller than their yield strain (see Fig. 11(b)) as the failure of specimens is controlled by the steel SHS chord.

3.4. Bearing capacity and the corresponding displacements

Fig. 12 demonstrates the effect of parameters on the bearing capacity (F_{ue}) of the specimens. As can be observed from Fig. 12(a), while keeping β and n value constant, the composite T-joints have an obviously higher F_{ue} than the corresponding steel T-joint, and 17.3~18.3 and 12.4~14.7 times improvement of F_{ue} are respectively achieved when $\beta = 0.3$ and β=0.5. For the composite T-joints having $\beta = 0.3$ and $n = 0.2$, F_{ue} changes a little with the variation of chord type and χ, seeing that the identical steel SHS brace determines the bearing capacity of these specimens and the difference may be caused by the variability of different specimen materials. In addition, for the composite T-joints having $\beta = 0.5$ and $n = 0.2$, a bigger χ of CFDST chord leads to a higher F_{ue} due again to the increased section modulus of inner steel SHS, and the specimen with CFDST chord leads to 5.7~11.7% larger P_{ue} than that with CFST chord. It is shown in Fig. 12(b) that, when β equals to 0.5, the composite T-joints having a larger n and χ generally have a higher F_{ue}, and in the case of $\chi = 0.3$ ($\chi = 0.5$) specimens with n of 0.2 and 0.4 have 2.0% (7.4%) and 11.9% (14.4%) larger F_{ue} than the corresponding specimen with n of 0.04. Similarly, in the case of $n = 0.04 \sim 0.4$, specimens with χ of 0.5 possesses 0.3~5.7% larger F_{ue} than the corresponding specimen with χ of 0.3. This is due mainly to the fact that, similar to the common square CFDST beam-columns [29], an increased concentric compression restraint can enhance the flexure-shear capacity of the composite members when n is within certain limits. Moreover, the inner tube of square CFDST chord with a larger χ leads to a larger section modulus and thus a larger moment resistance; however, the improvement is limited owing to the second-order effect and difference in material property.

Fig. 13 demonstrates the change of $\Delta_{\mathrm{mc,ue}}$ and $\Delta_{\mathrm{tb,ue}}$ of all specimens. As can be seen in Fig. 13 and Table 2, $\Delta_{\mathrm{tb,ue}}$ are larger than $\Delta_{\mathrm{mc,ue}}$ owing to the compression deformation of brace and chord beneath the brace. It is shown in Fig. 13(a) that, $\Delta_{\mathrm{mc,ue}}$ and $\Delta_{\mathrm{tb,ue}}$ of the composite T-joints are also obviously larger than those of their steel counterparts due again to the contribution of concrete and/or inner tube in the chord, and about 1.4~1.9 (2.1~2.2) and 12.2~15.1 (19.2~19.7) times of $\Delta_{\mathrm{mc,ue}}$ ($\Delta_{\mathrm{tb,ue}}$) are respectively achieved when $\beta = 0.3$ and β=0.5. Moreover, for the composite T-joints having $\beta = 0.3$ as well as $n = 0.2$, $\Delta_{\mathrm{mc,ue}}$ and $\Delta_{\mathrm{tb,ue}}$ of T-joint with CFDST chord having χ of 0.3 and 0.5 are larger than those of T-joint with CFDST chord as the flexural stiffness of the CFDST chord is enhanced owing to the presence of the inner tube, which produces a decreased chord vertical displacement and an increased the chord restraint to the vertical displacement of brace for the specimens having brace failure. However, for the composite T-joints having $\beta = 0.5$ as well as $n = 0.2$, the chord type generally has a moderate effect on the change of $\Delta_{\mathrm{mc,ue}}$ and $\Delta_{\mathrm{tb,ue}}$. It can be observed from Fig. 13(b) that, $\Delta_{\mathrm{mc,ue}}$ and $\Delta_{\mathrm{tb,ue}}$ generally decrease with increase of n and χ has a moderate impact on $\Delta_{\mathrm{mc,ue}}$ and $\Delta_{\mathrm{tb,ue}}$ except for the specimens with $n = 0.04$. When n is increased from 0.04 to 0.4 whilst χ is maintained the same, 62.8~67% (χ=0.3) and 56.0~60.4% (χ=0.5) lower $\Delta_{\mathrm{mc,ue}}$ as well as 57.4~59.4% (χ=0.3) and 48.9~55.3% (χ=0.5) lower $\Delta_{\mathrm{tb,ue}}$ are produced. This is due to the fact that the chord of the composite T-joints having a larger n reaches the yield or failure earlier.

4. Finite element (FE) simulation

To capture the static behaviour of the square CFDST chord to steel SHS brace T-joints, a finite element (FE) model was established based on the nonlinear analysis tool ABAQUS [31].

4.1. Description of the FE model

Four-node reduced integrated shell elements (S4R) were adopted for the modelling of steel SHSs in the T-joints, and eight-node reduced integrated three-dimensional solid elements (C3D8R) were employed for the simulating of the concrete in the composite chord and the endplates.

Element division of the FE model of the composite T-joints was accomplished by the structured meshing methods in ABAQUS [31], and based on the balance of computational accuracy and convergence rate, a reasonable element density was obtained by attempting different mesh sizes. Moreover, there were dense meshing as well as alignment of mesh nodes in the area where the brace was connected to the chord, as indicated in Fig. 14.

The steel SHSs in the T-joints were modelled by the elastic-plastic model. The measured modulus of elasticity (E_s) and Poisson's ratio (μ_s) in Table 1 were taken as the elastic properties of steel. The plasticity of steel was represented in the form of true stress and logarithmic plastic strain tabulated data, which was converted using the engineering stress versus strain relationship in [32]. Furthermore, in order to simplify the calculation reasonably, the endplates of the brace and chord were set to be a type of rigid material with modulus of elasticity and Poisson's ratio of 1.0×10^{12} N/mm^2 and 0.00001, respectively.

The concrete in the composite chord was simulated by the concrete damage plasticity (CDP) model. The modulus of elasticity of concrete (E_c) was equal to $4730\sqrt{f_\mathrm{c}'}$ [33] together with the Poisson's ratio (μ_c) of 0.2 [34] in the elastic stage, where f_c' is the cylindrical compressive strength. Within the plastic stage, the concrete subject to compression was depicted by the stress-strain relationship in [35] by using the confinement factor ξ $(= \alpha_\mathrm{n} \cdot f_\mathrm{yo}/f_\mathrm{ck})$ as main variable, where α_n is the nominal steel ratio of a composite chord, f_yo is the yield strength of outer steel SHS, and f_ck is the characteristic compressive strength of concrete [5, 29]. The tension-stiffening effect of concrete subject to tension was described by the fracture energy cracking model, in which the peak tensile stress equals to $0.1f_\mathrm{c}'$ and the fracture energy (G_f) suggested in [34] was employed. To characterize the concrete damage induced by the deformation in the plastic phase, the evolutions of compression (tension) damage variable were computed using the equations suggested in [36].

The FE model of the composite T-joints had five independent parts, i.e. two steel tubes of the chord, steel SHS of the brace, the concrete in the chord, and endplates of the chord and brace. The interactions between two steel tubes and the concrete in the chord was captured by the surface-to-surface contacts, which were also used between three parts of the chord and the corresponding endplates. The normal and tangential direction of the interface were respectively defined as a hard contact and a Coulomb friction model with the friction coefficients of 0.6 [37]. In addition, the interfacial performance between the brace and the outer steel tube of the chord or its endplate was modelled by the 'TIE' contact.

Fig. 14 illustrates the boundary conditions used in the FE model. The plate hinges in the experiments (shown as in Fig. 3) were simulated by defining two reference points (Pr1 and Pr2), which were coaxial with the centroid of chord section, and there was a distance of 115 mm between the chord endplate and the corresponding reference point. The sphere hinge on the actuator (also shown as in Fig. 3) was modelled by the third reference point (Pr3), which was located in the plane of symmetry along Y axis, and there was a distance of 600 mm between the brace endplate and the Pr3. The restricted translations included: three directions of Pr1 (U_X=U_Y=U_Z=0), two directions of Pr2 (U_X=U_Z=0) and one direction of Pr3 (U_X=0), and all three reference points had the restricted rotations in two directions (UR_Y=UR_Z=0). In addition, to reproduce the imperfections during the processing and testing of the specimens, an initial eccentricity (e_i) of $L_\mathrm{be}/1000$ with respect to the symmetry axis along X-axis was applied to the Pr3, as shown in Fig. 14, where L_be is the brace effective length. Firstly, the constant axial compressive load (N_0) was applied to the Pr2, and then the displacements along the Z-axis were acted on the Pr3 until the modelling ends.

To further investigate the effect of welds, another FE model with the welds between the brace and the outer tube of the chord was also built. In this model, the welds were defined as an elastic material with size (w), yield strength, modulus of elasticity and Poisson's ratio of $1.5t_\mathrm{b}$, 400 MPa, 2.06×10^5 N/mm^2 and 0.3, respectively, and were simulated by C3D8R elments. The 'TIE' contact was adopted to model the interface between the welds and the brace or the outer tube of the chord. The comparison of FE simulation results of the T-joint specimens with and without welds is demonstrated in Fig. 15. It can be observed that the influence of the welds on the static performance of the T-joint specimens is small, and thus the welds between the brace and the outer tube of the chord were not considered in the FE model.

4.2. Verifications of the FE modelling

The FE modelling results are evaluated against the experimental observations. Fig. 16 illustrates the simulated failure patterns. The contrast between Fig. 16(a) and Fig. 4 shows that, the simulated buckling pattern and positions of top flange and webs of outer chord tube and overall deflection shape of chord in the composite T-joints having β of 0.5, the local buckling of brace in the composite T-joints having β of 0.3, and the yielding of top flange and buckling of webs of chord in the steel T-joints generally accord well with the experimental phenomena. The contrast between Fig. 16(b) and

Fig. 5 indicates that, for the infilled concrete, the modelled distribution of main plastic strains (PE) and the position where the maximum PE occurs generally accord well with the observed pattern and location of compressive crushing and tensile cracking in the tests. As can be seen from Fig. 16(c) and Fig. 6, a relatively good correlation between the computed overall deflection and/or local buckling of inner tube of the CFDST chord and the experimental results. The simulated failure patterns are also given in Table 2.

Fig. 17 demonstrates the contrast between the numerical and measured $F-\Delta_{\mathrm{tb}}$ curves, where the experimental data of steel SHS chord to square CFDST X-joints with the chord end free have also been adopted to increase the reliability of the FE model. It is shown that, the computed developing trend of $F-\Delta_{\mathrm{tb}}$ curves are generally accord well with the measured ones. However, the numerical $F-\Delta_{\mathrm{tb}}$ curves of the composite T-joints have an apparently higher initial slope than the experiemntal results. There are three main reasons for this: 1) the FE model cannot reproduce the imperceptible gaps between different parts, 2) the joints with a larger size have more defects than the specimens having a smaller size for conducting a material test, and 3) it is impossible to invariably maintain the ideal concentric compression of the chord in the experiment. The contrast between the numerical and measured $F-\varepsilon_{\mathrm{L}}(\varepsilon_{\mathrm{T}})$ relationship is indicated in Fig. 18, where ε_{L} and ε_{T} respectively stand for longitudinal and transverse strain. It is shown that the slope of the numerical $F-\varepsilon_{\mathrm{L}}(\varepsilon_{\mathrm{T}})$ curves is generally close to that of the experimental results, and compared to the numerical $F-\Delta_{\mathrm{tb}}$ curves, the $F-\varepsilon_{\mathrm{L}}(\varepsilon_{\mathrm{T}})$ curves have a better computational initial slope. This can be explained that, the strain measurement is carried out in a very small range, while the displacement measurement is relative to the chord span, and the former is less affected by the aforementioned three types of defects. The computed bearing capacity of the T-joints by FE model ($F_{\mathrm{ufe,j}}$) and $F_{\mathrm{ufe,j}}/F_{\mathrm{ue,j}}$ values are given in Table 2, and Fig. 19 shows the contrast between $F_{\mathrm{ufe,j}}$ and $F_{\mathrm{ue,j}}$. The comparison demonstrates that, the computational results are generally reasonable, seeing that $F_{\mathrm{ufe,j}}/F_{\mathrm{ue,j}}$ values have a mean and standard deviation (SD) of 0.950 and 0.063, respectively.

Although there is a certain descrepancy in the initial slope between the computed and recorded force versus displacement (strain) relationship, the simulated failure patterns, bearing capacity and displacement (strain) evolution generally exhibit a good correlation with the experimental observations. Therefore, the FE model can be regarded as a good predictor for reproducing the performance of the square CFDST chord to steel SHS brace T-joints.

5. Simplified formulae for computing the bearing capacity

The above test and FE modelling results indicate that, the performance of square CFDST chord to steel SHS brace T-joints with β of 0.3 and 0.5 is mainly dominated by that of individual steel SHS brace and square CFDST chord, respectively, and thus the bearing capacity of the composite T-joints should be associated with that of their chord and brace. To find out the connection between the bearing capacity of individual components and that of the composite T-joints, FE simulations on the behaviour of the individual brace and chord under static loading were further performed. Figs. 20(a) and (b) shows the FE model of the individual components. The individual steel SHS brace had the same conditions as that in the model of joints with the vertical displacements applied from the top and an initial eccentricity of $L_{\mathrm{be}}/1000$, except that all degree-of-freedoms of the bottom cross-section connected with the chord in the joint were restricted. It should be pointed out that, in order to simplify the FE modelling and facilitate the future design, the flexural deformation of the top wall of the chord connected with the bottom cross-section of steel SHS brace was temporarily ignored for the individual brace model, as the flexural deformation of the top wall of the chord is usually very small in reality, unless significant lateral displacement of the brace is presented after reaching the bearing capacity of the joint. Moreover, the individual square CFDST chord also possessed the same conditions as that in the model of joints, except that the compression from the brace was replaced by a compressive square area with the same width as the outer width of the brace, and the lateral displacements were applied by a reference point (Pr3) coupled with the loading area. Figs. 20(c) and (d) demonstrate the simulated failure pattern of typical individual components. It can be observed from the comparison between Figs. 20(c) and (d) and Figs. 4 and 16(a) that, the individual brace and chord have the same failure patterns as those of the corresponding components in the composite T-joints with $\beta = 0.3$ and $\beta = 0.5$. The contrast between the computed bearing capacity of the composite T-joints together with the individual components and F_{ue} is summarised in Table 3, in which $F_{\mathrm{ufe,b}}$ and $F_{\mathrm{ufe,c}}$ respectively represent the bearing capacity of individual brace and chord computed by the FE model, and $F_{\mathrm{ufe,bc}}$ equals to the minimum of $F_{\mathrm{ufe,b}}$ and $F_{\mathrm{ufe,c}}$. The results indicate that, $F_{\mathrm{ufe,bc}}$ and $F_{\mathrm{ufe,j}}$ are very close and have the similar statistical indexes compared to $F_{\mathrm{ue,j}}$, which means that the bearing capacity of the composite T-joints is determined by the minimum bearing capacity of their individual components.

The FE model was employed for extensive parametric analysis to further confirm the above viewpoint, and the calculating parameters included: $b_{\mathrm{o}} = 400\ \mathrm{mm}$, $\beta = 0.1{\sim}0.9$, $\chi = 0{\sim}0.75$, $n = 0{\sim}0.75$, $\alpha_{\mathrm{n}} = 0.05{\sim}0.2$, slenderness ratio of the square CFDST chord $\lambda = 10{\sim}80$, yield strength of steel SHS brace (inner and outer tube in the chord) f_{yb}(f_{yi}, f_{yo}) =235~460 MPa, f_{c}' =25~75 MPa, $b_{\mathrm{i}}/t_{\mathrm{i}} = 20{\sim}80$, $b_{\mathrm{b}}/t_{\mathrm{b}} = 10{\sim}30$, and length to width ratio of brace $l_{\mathrm{b}}/b_{\mathrm{b}} = 5{\sim}20$. A total of 239 joint models covering the parameter range were simulated.

To facilitate analysis, a bearing capacity factor (K_1) is defined as follows:

$$K_1 = \frac{F_{\mathrm{ufe,j}}}{\min\{F_{\mathrm{ufe,b}}\,, F_{\mathrm{ufe,c}}\}} \tag{5}$$

The variation of K_1 with $F_{\mathrm{ufe,b}}/F_{\mathrm{ufe,c}}$ values is demonstrated in Fig. 21. The results indicate that K_1 values are from 0.962 to 1.043, with mean and SD of 0.996 and 0.011, respectively. Particularly, K_1 values of the joint having failure of brace (i.e. $K_1 = F_{\mathrm{ufe,j}}/F_{\mathrm{ufe,b}}$) are from 0.986 to 1.043, with mean and SD of 1.008 and 0.010, respectively. The comparison results in Table 3 and Fig. 21 demonstrate that, within the range of the experimental and FE simulation parameters of this study, it is generally feasible to assume that the bottom cross-section of the steel SHS brace connected with the chord in the joint is under an ideal rigid restriction while calculating the bearing capacity of individual steel SHS brace.

Currently, simplified equations for the bearing capacity of the steel SHS members can be found in the design codes, e.g. EN 1993-1-1 [27]; however, there is no specific method for square CFDST members subjected to the combined concentric compression as well as lateral local compression acting on the mid-span (see Fig. 20(b)). Therefore, it is necessary to establish the connection between the square CFDST members subjected to the combined concentric compression as well as lateral local compression acting on the mid-span and those subject to the combination of compression, flexure and shear, because the formulae for the bearing capacity prediction of the latter can be obtained in the literature [29, 38]. Fig. 22 demonstrates the comparison of square CFDST members under different loading conditions, where CFS represents the combination of compression, flexure and shear. In the FE modelling, the square CFDST member under CFS had the same conditions as those of the individual square CFDST chord in the T-joint, except that there is no square loading area and the mid-span lateral displacements were applied by a rigid plate fixed with the cross-section. The results indicate that, square CFDST members subject to CFS have different force-displacement curves (Fig. 22(a)) and failure patterns (Fig. 22(b)) compared to those under the combined concentric compression and lateral local compression at the mid-span. The individual chords with a bigger brace-to-chord width ratio (β) have a closer performance to the corresponding members under CFS, and the individual chords with a very small β (e.g. $\beta = 0.1$) are more prone to joint zone failure.

Another bearing capacity factor (K_0) is thus defined to measure the difference in bearing capacity of square CFDST members under the above two loading conditions, and the equation is:

$$K_0 = \frac{F_{\mathrm{ufe,c}}}{F_{\mathrm{ufe,0}}} \tag{6}$$

where, $F_{\mathrm{ufe,0}}$ is the numerical lateral bearing capacity of square CFDST members under the combination of compression, flexure and shear.

It is observed from the simulated results that, the bearing capacity factor (K_0) is mainly affected by β, χ and λ no matter what pattern of failure occurs to the square CFDST chord, and other parameters only have slight influence on K_0. Fig. 23 demonstrates the influence of β, χ and λ on K_0. According to a large number of parametric analysis results, the simplified formulae for K_0 is obtained based on regression analysis method:

$$K_0 = [0.12\ln(\beta) + 1.08] \cdot (p_1 \cdot \chi^2 + p_2 \cdot \chi + p_3) \cdot \left(q_1 + q_2 \cdot e^{-0.025\lambda/q_3}\right) \tag{7}$$

where, $p_{i(i=1,2,3)}$ and $q_{i(i=1,2,3)}$ are calculating parameters, $p_1 = -3.43\beta^2 + 5.34\beta - 2.02$, $p_2 = 1.33\beta^2 - 1.96\beta + 0.67$, $p_3 = -0.23\beta^2 - 0.26\beta + 1.04$, $q_1 = 1.59\beta^2 - 1.28\beta + 1.51$, $q_2 = 5.34\beta^2 - 1.37\beta - 1.7$, and $q_3 = 1.15\beta^2 - 1.46\beta + 0.56$.

The calculated K_0 using Eq. (7) are also presented in Fig. 23. It can be seen that, Eq. (7) is suitable for accurately calculating the bearing capacity coefficient K_0.

According to Eqs. (5) to (7), the bearing capacity of the square CFDST chord to steel SHS brace T-joints ($F_{\mathrm{u,j}}$) can therefore be derived as follows:

$$F_{\mathrm{u,j}} = \begin{cases} F_{\mathrm{u,b}} & (\theta < 1) \\ K_0 \cdot F_{\mathrm{u,0}} & (\theta \geq 1) \end{cases} \tag{8}$$

where, $F_{\mathrm{u,b}}$ is the stability bearing capacity of individual SHS brace under concentric compression based on the formulae in [27]; $F_{\mathrm{u,0}}$ is the lateral bearing capacity of individual square CFDST chord subject to CFS; and the parameter $\theta(= F_{\mathrm{u,b}}/(K_0 \cdot F_{\mathrm{u,0}}))$ should be calculated according to the standard value of material strength in the design. In this study, the design formulae in [29, 38] are adopted to compute $F_{\mathrm{u,0}}$, and the detailed formulae are as follows:

$$\begin{cases} \left(\frac{1}{\varphi} \cdot \frac{N_0}{N_{\mathrm{u}}} + \frac{a}{d} \cdot \frac{M}{M_{\mathrm{u}}}\right)^{2.4} + \left(\frac{V}{V_{\mathrm{u}}}\right)^2 = 1 & \left(\frac{N_0}{N_{\mathrm{u}}} \geq 2\varphi^3 \cdot \eta_0 \cdot \sqrt[2.4]{1 - \left(\frac{V}{V_{\mathrm{u}}}\right)^2}\right) \\ \left(-b \cdot \frac{N_0^2}{N_{\mathrm{u}}^2} - c \cdot \frac{N_0}{N_{\mathrm{u}}} + \frac{1}{d} \cdot \frac{M}{M_{\mathrm{u}}}\right)^{2.4} + \left(\frac{V}{V_{\mathrm{u}}}\right)^2 = 1 & \left(\frac{N_0}{N_{\mathrm{u}}} < 2\varphi^3 \cdot \eta_0 \cdot \sqrt[2.4]{1 - \left(\frac{V}{V_{\mathrm{u}}}\right)^2}\right) \end{cases} \tag{9}$$

where, φ is the stability coefficient; N_{u}, M_{u} and V_{u} are the sectional strength subject to concentric compression, flexure and shear, respectively [29, 38]; a, b, c and η_0 are the intermediate variables; d is the factor considering the second-order effect; M is the external moment calculated by $F_{\mathrm{u,0}} \cdot L_{\mathrm{ce}}/4$; and V is the external shear force equal to $F_{\mathrm{u,0}}/2$.

Fig. 24 demonstrates the contrast between the simplified bearing capacities ($F_{\mathrm{us,j}}$) using Eq. (8) and the numerical results ($F_{\mathrm{ufe,j}}$), and the mean and SD of $F_{\mathrm{us,j}}/F_{\mathrm{ufe,j}}$ values are equal to 0.962 and 0.052, respectively. The simplified bearing capacities ($F_{\mathrm{us,j}}$) using Eq. (8) are further compared to the experimental results ($F_{\mathrm{ue,j}}$) in Fig. 25. The mean and SD of $F_{\mathrm{us,j}}/F_{\mathrm{ue,j}}$ values are equal to 0.859 and

0.072, respectively. It can be observed from the above comparison that the suggested simplified equations are capable of effectively computing the bearing capacity of the square CFDST chord to steel SHS brace T-joints. It should be noted that, while using Eq. (8) in design of composite T-joints, the chord concrete of higher strength class should be used in line with higher grade steel tube [5] to ensure the composite actions between steel tubes and the sandwiched concrete, and the buckling resistance of the SHS brace should match the lateral capacity of the CFDST chords under CFS.

6. Conclusions

The performance of square CFDST chord to steel SHS brace T-joints under static loading are experimentally and numerically investigated in this study, and the main conclusions are as follows:

1) Compared to bare steel SHS T-joints, the composite T-joints with square CFDST/CFST chord have better static performance and significantly different failure patterns.

2) For the composite T-joints having destruction of chord (i.e. $\beta = 0.5$), the local buckling of top flange and webs of outer chord tube and inward local bucking and overall deflection of inner chord tube, together with crushing under compression and cracking under tension of the concrete between the tubes, are observed. For the composite T-joints having destruction of brace (i.e. $\beta = 0.3$), the local buckling near the top and bottom section of brace appears.

3) For the composite T-joints having destruction of chord, a bigger n results in a higher initial slope of force-displacement (strain) relationship and a larger bearing capacity (F_{ue}), and generally specimens with n of 0.2 and 0.4 have 2.0-7.4% and 11.9-14.4% larger F_{ue} than those with n of 0.04. In addition, a larger n and χ leads to a higher descending slope of load versus deformation curves after achieving F_{ue}. For the composite T-joints having destruction of brace, the chord type has no evident impact on the initial and falling slope of force-displacement (strain) relationship.

4) Under the same β and n values, the composite T-joints possess a significantly larger initial slope of the force-displacement (strain) relationship and F_{ue}, and a quite smaller falling slope of force-displacement (strain) relationship after achieving F_{ue} than the corresponding steel T-joints. Generally, the composite T-joints having $\beta = 0.3$ and β=0.5 respectively result in 17.3~18.3 and

12.4~14.7 times improvement of F_{ue} over the corresponding steel T-joints.

5) The FE model is validated by the experimental results. The simplified formulae for computing the bearing capacity of the composite T-joints was developed, and the precision of the suggested equations is validated by numerical and experimental results. Therefore, the simplified formulae can be used for future design.

Declaration of Competing Interest

The authors declare that they have no known competing financial interests or personal relationships that could have appeared to influence the work reported in this paper.

Acknowledgements

The studies in this paper are financially supported by the National Natural Science Foundation of China (Project 51678105). The financial support is gratefully acknowledged. The authors also wish to thank Mr. Yue Ma for his assistance in the experimental tests.

References:

[1] Wardenier J, Packer JA, Zhao XL, van der Vegte GJ. Hollow sections in structural applications. Netherlands: Bouwen met Staal; 2010.

[2] Packer JA. Concrete-filled HSS connections. Journal of Structural Engineering ASCE 1995;121(3):458-67.

[3] Ayough P, Sulong RNH, Ibrahim Z, Hsiao PC. Nonlinear analysis of square concrete-filled double-skin steel tubular columns under axial compression. Engineering Structures 2020;216: 110678.

[4] Yang YF, Han LH, Sun BH. Experimental behaviour of partially loaded concrete filled double-skin steel tube (CFDST) sections. Journal of Constructional Steel Research 2012;71:63-73.

[5] Han LH, Lam D, Nethercot DA. Design guide for concrete-filled double skin steel tubular structures. UK: CRC Press; 2018.

[6] Chen J, Chen J, Jin WL. Experiment investigation of stress concentration factor of concrete-filled tubular T joints. Journal of Constructional Steel Research 2010;66(12):1510-15.

[7] Chen J, Zhang DW, Jin WL. Concrete-filled steel and steel tubular T-joints under cyclic in-plane bending. Advances in Structural Engineering 2015;18(12):2207-16.

[8] Liu H, Shao Y, Lu N, Wang Q. Hysteresis of concrete-filled circular tubular (CFCT) T-joints under axial load. Steel and Composite Structures 2015;18(3):739-56.

[9] Feng R, Young B. Tests of concrete-filled stainless steel tubular T-joints. Journal of Constructional Steel Research 2008;64(11):1283-93.

[10] Feng R, Young B. Behaviour of concrete-filled stainless steel tubular X-joints subjected to compression. Thin-Walled Structures 2009;47(4):365-74.

[11] Chen Y, Feng R, Ruan X. Behaviour of steel-concrete-steel SHS X-joints under axial compression. Journal of Constructional Steel Research 2016;122:469-87.

[12] Yang YF, Shi C, Hou C. Experimental and numerical study on static behaviour of uniplanar CFDST-CHS T-joints. Journal of Constructional Steel Research 2020;173:106250.

[13] Hou C, Han LH, Mu TM. Behaviour of CFDST chord to CHS brace composite K-joints: Experiments. Journal of Constructional Steel Research 2017;135:97-109.

[14] Huang W, Fenu L, Chen B, Briseghella B. Experimental study on K-joints of concrete-filled steel tubular truss structures. Journal of Constructional Steel Research 2015;107:182-93.

[15] Mashiri FR, Zhao XL. Square hollow section (SHS) T-joints with concrete-filled chords subjected to in-plane fatigue loading in the brace. Thin-Walled Structures 2010;48(2):150-8.

[16] Qian X, Jitpairod K, Marshall P, Swaddiwudhipong S, Ou Z, Zhang Y, Pradana MR. Fatigue and residual strength of concrete-filled tubular X-joints with full capacity welds. Journal of Constructional Steel Research 2014;100:21-35.

[17] Sakai Y, Hosaka T, Isoe A, Ichikawa A, Mitsuki K. Experiments on concrete filled and reinforced tubular K-joints of truss girder. Journal of Constructional Steel Research 2004;60(3-5):683-99.

[18] Udomworarat P, Miki C, Ichikawa A, Komechi M, Mitsuki K, Hosaka T. Fatigue performance of composites tubular K-joints for truss type bridge. Structural Engineering/Earthquake Engineering 2002;19(2):65-79.

[19] Udomworarat P, Miki C, Ichikawa A, Sasaki E, Sakamoyo T, Mitsuki K, Hosaka T. Fatigue and ultimate strengths of concrete filled tubular K-joints on truss girder. Journal of Structural Engineering 2000;46A:1627-35.

[20] Xu F, Chen J, Jin WL. Experimental investigation and design of concrete-filled steel tubular CHS connections. Journal of Structural Engineering ASCE 2015;141(2):04014106.

[21] Xu F, Chen J, Jin WL. Experimental investigation of SCF distribution for thin-walled concrete-filled CHS joints under axial tension loading. Thin-Walled Structures 2015;93:149-57.

[22] Hou C, Han LH. Analytical behaviour of CFDST chord to CHS brace composite K-joints. Journal of Constructional Steel Research 2017;128:618-32.

[23] Kim IG, Chung CH, Shim CS, Kim YJ. Stress concentration factors of N-joints of concrete-filled tubes subjected to axial loads. International Journal of Steel Structures 2014;14(1):1-11.

[24] Musa IA, Mashiri FR, Zhu X. Parametric study and equation of the maximum SCF for concrete filled steel tubular T-joints under axial tension. Thin-Walled Structures 2018;129:145-56.

[25] Zheng J, Nakamura S, Ge Y, Chen K, Wu Q. Formulation of stress concentration factors for concrete-filled steel tubular (CFST) T-joints under axial force in the brace. Engineering Structures 2018;170:103-17.

[26] Xu F, Chen J, Jin WL. Punching shear failure of concrete-filled steel tubular CHS connections. Journal of Constructional Steel Research 2016;124:113-21.

[27] EN 1993-1-1. Eurocode 3: Design of steel structures, Part 1-1: General rules and rules for buildings. Comité Européen de Normalisation (CEN), Brussels, Belgium, 2005.

[28] ANSI/AISC 360. Specification for structural steel buildings. American Institute of Steel Construction, Chicago, USA, 2016.

[29] Tao Z, Han LH. Behaviour of concrete-filled double skin rectangular steel tubular beam-columns. Journal of Constructional Steel Research 2006;62(7):631-46.

[30] Zhao XL. Deformation limit and ultimate strength of welded T-joints in cold-formed RHS sections. Journal of Constructional Steel Research 2000;53(2):149-65.

[31] Simulia. ABAQUS analysis user’s guide, version 6.14. Providence, RI: Dassault Systèmes Simulia Corp., 2014.

[32] Abdel-Rahman N, Sivakumaran KS. Material properties models for analysis of cold-formed steel members. Journal of Structural Engineering ASCE 1997;123(9):1135-43.

[33] ACI Committee 318. Building code requirements for structural concrete (ACI 318-19) and commentary. American Concrete Institute, Detroit, USA, 2019.

[34] FIB. Fib model code for concrete structures 2010. Fédération Internationale du Béton, Ernst & Sohn, Berlin, Germany, 2013.

[35] Han LH, Yao GH, Tao Z. Performance of concrete-filled thin-walled steel tubes under pure torsion. Thin-Walled Structures 2007;45(1):24-36.

[36] Birtel V, Mark P. Parameterised finite element modelling of RC beam shear failure. In: Proceedings of the 2006 ABAQUS Users' Conference; 2006, p. 95-108.

[37] Yang YF, Bie XM, Hou C, Han LH. Analytical behaviour and design of square CFDST subjected to local bearing force. Journal of Constructional Steel Research 2019;159: 198-214.

[38] China Civil Engineering Society (CCES). Technical specification for concrete-filled double skin steel tubular structures (T/CCES 7-2020). Beijing: China Architecture & Building Press; 2020. (in Chinese)

Figures:

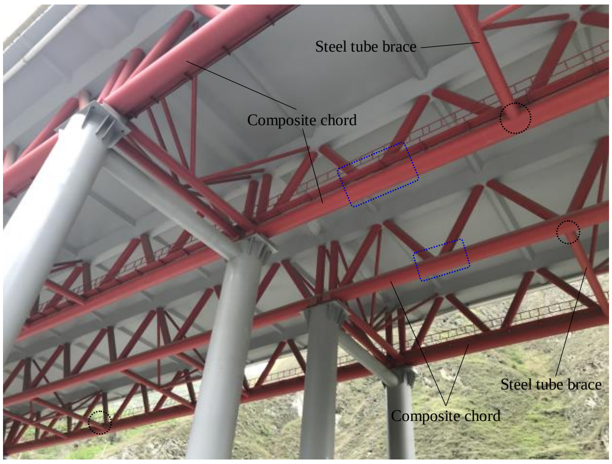

(a) On-sight photo (with pre-stressed chords)

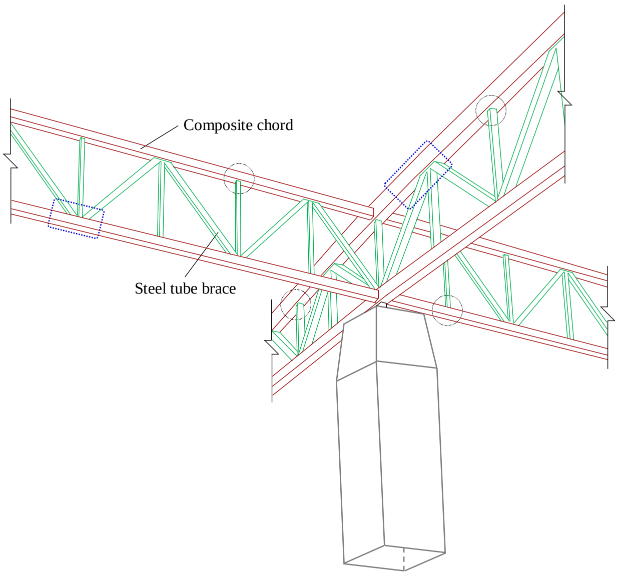

(b) Schematic view

Fig. 1. Typical on-sight photo and schematic view of composite tubular joints.

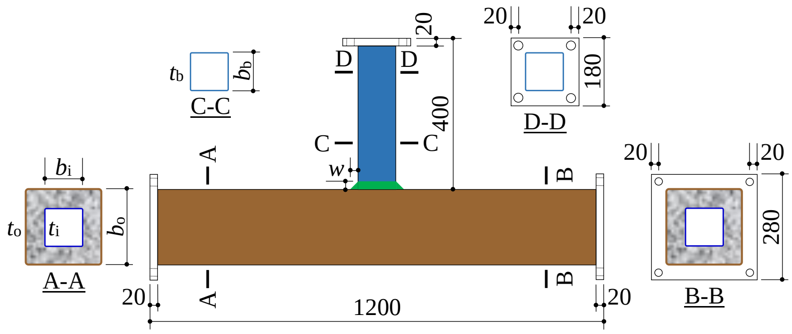

Fig. 2. Configurations of the specimens

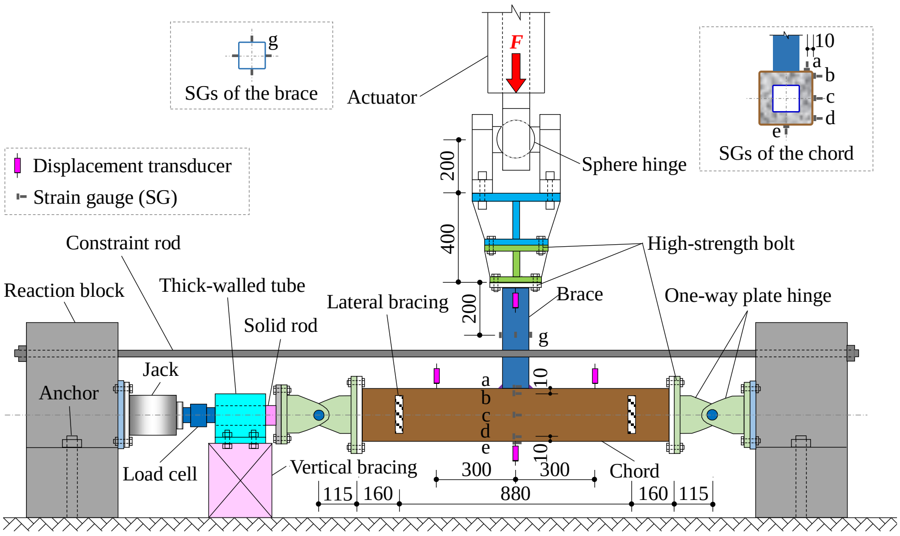

(a) Schematic view (unit: mm)

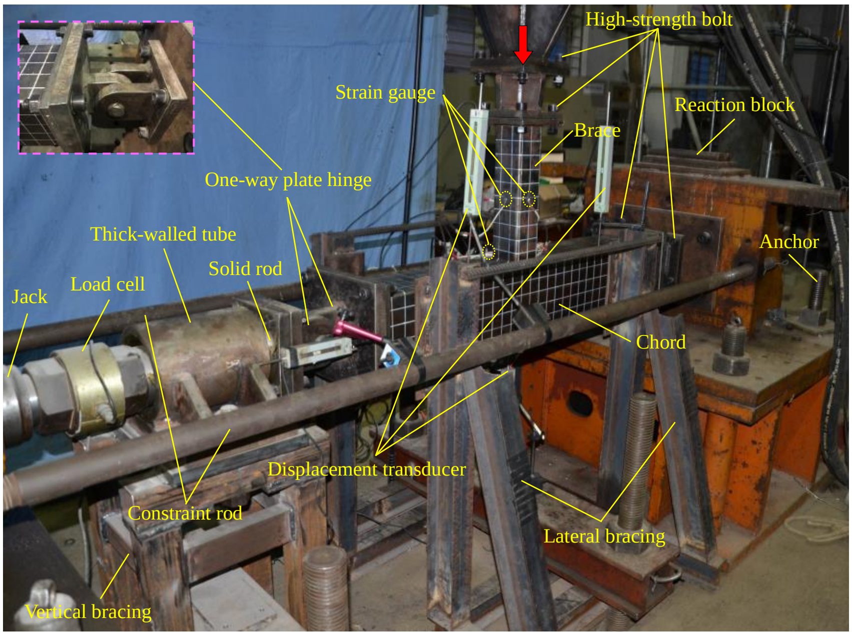

(b) Actual situation

Fig. 3. Test rig and measuring instruments

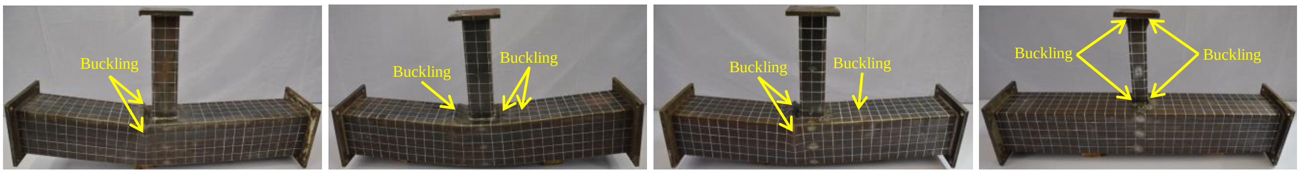

(1) C0.3-0.5-0.04 (2) C0.3-0.5-0.2 (3) C0.3-0.5-0.4 (4) C0.3-0.3-0.2

(a) CFDST chord (χ=0.3)

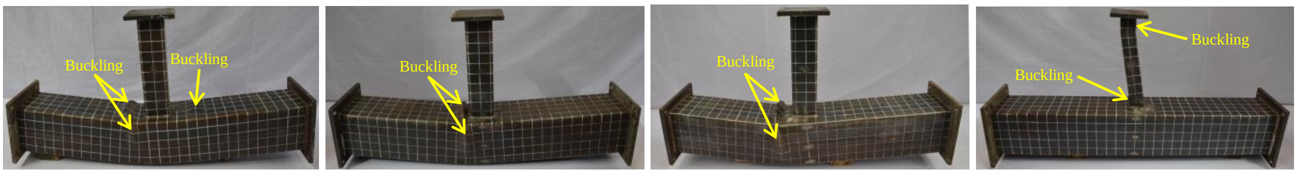

(1) C0.5-0.5-0.04 (2) C0.5-0.5-0.2 (3) C0.5-0.5-0.4 (4) C0.5-0.3-0.02

(b) CFDST chord (χ=0.5)

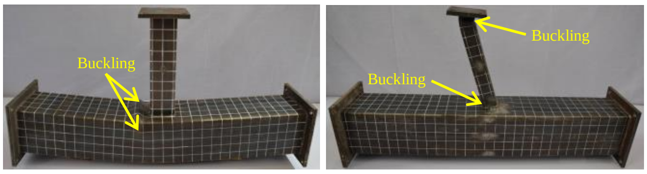

(1) C-0.5-0.2 (2) C-0.3-0.2

(c) CFST chord

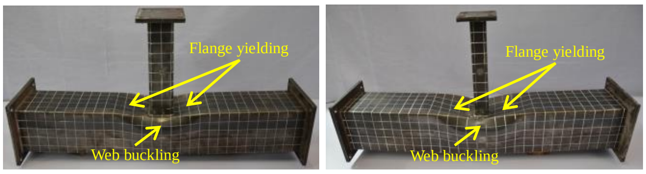

(1) S-0.5-0.2 (2) S-0.3-0.2

(d) Steel SHS chord

Fig. 4. Failure pattern of the specimens

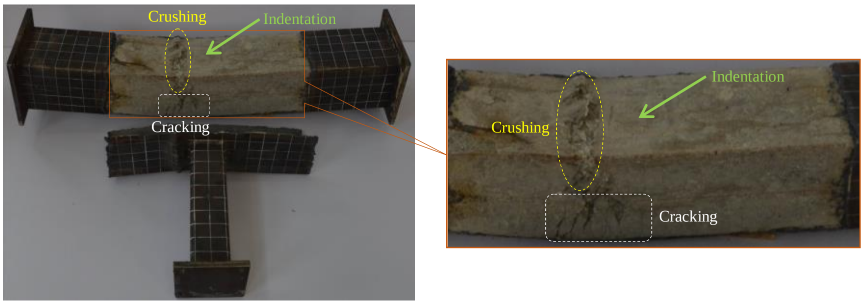

(a) C0.3-0.5-0.04

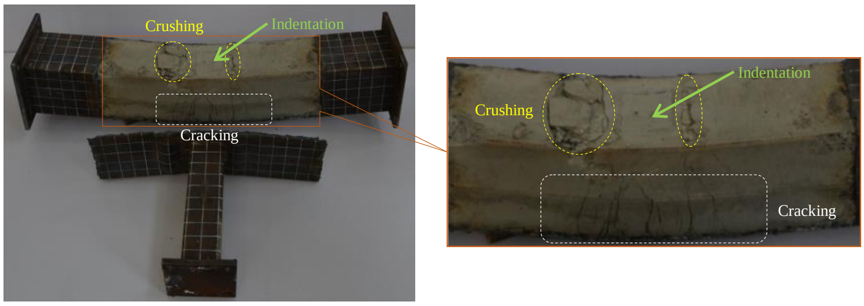

(b) C0.3-0.5-0.2

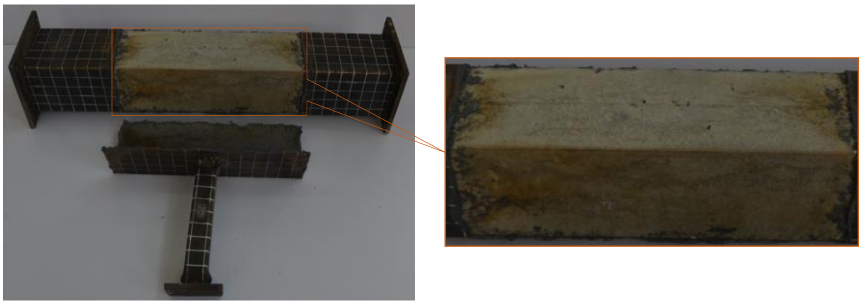

(c) C0.3-0.3-0.2

Fig. 5. Representative failure pattern of the concrete in the composite chord

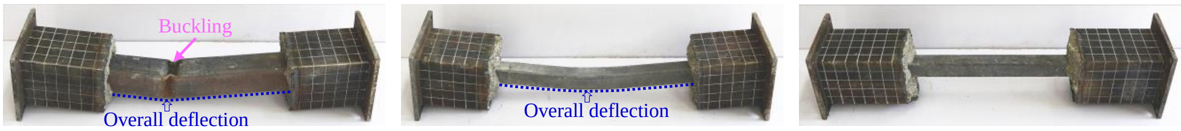

(a) χ=0.5, β=0.5 (b) χ=0.3, β=0.5 (c) χ=0.3, β=0.3

Fig. 6. Typical failure pattern of inner steel SHS in the CFDST chord

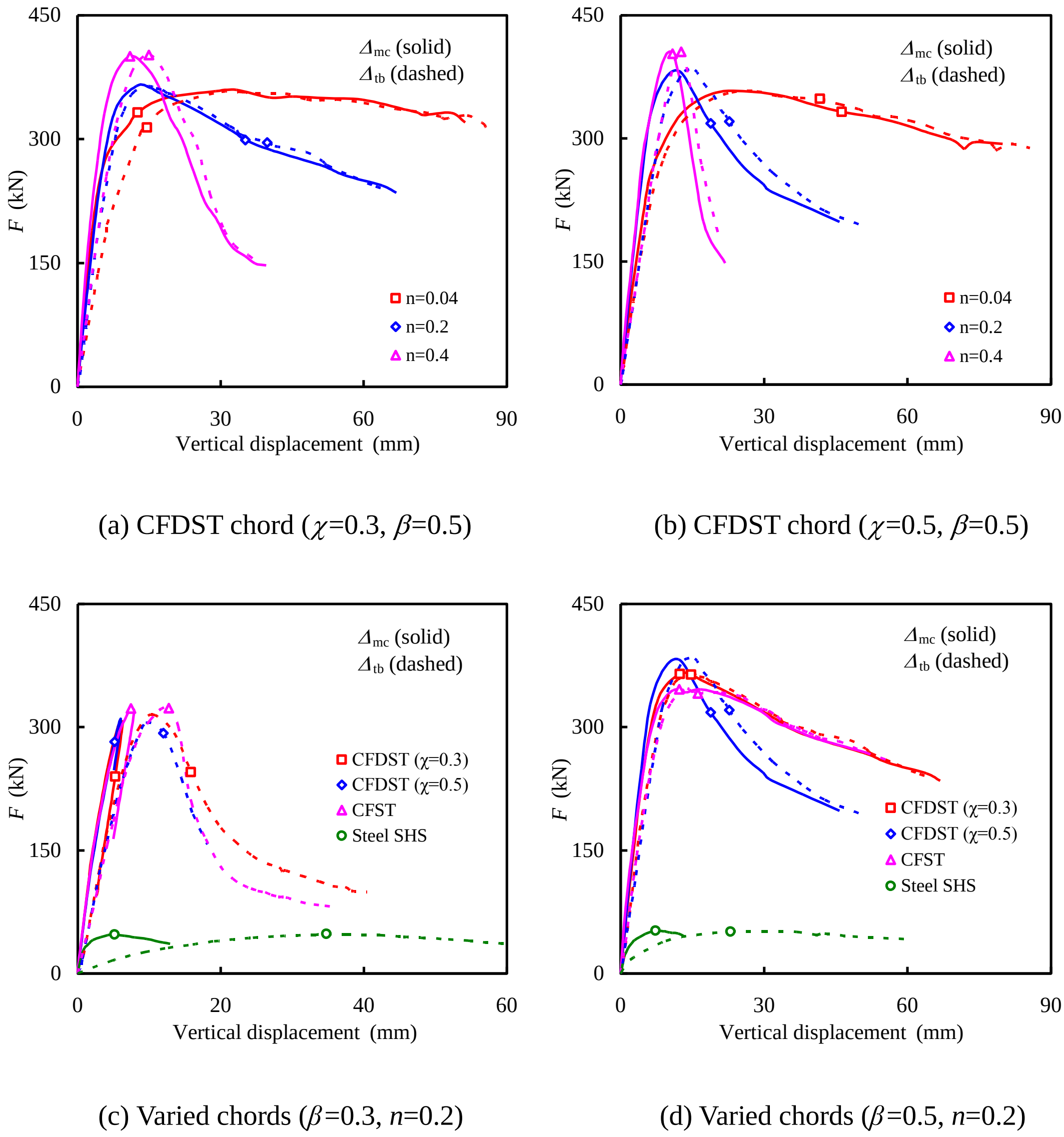

(a) CFDST chord (χ=0.3, β=0.5)

(b) CFDST chord (χ=0.5, β=0.5)

(c) Varied chords (β=0.3, n=0.2)

(d) Varied chords (β=0.5, n=0.2)

Fig. 7. Force versus vertical displacement relationship of the specimens

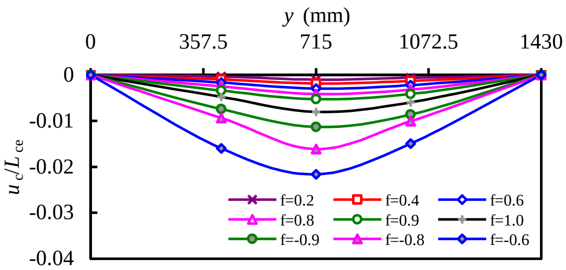

(a) C0.5-0.5-0.2

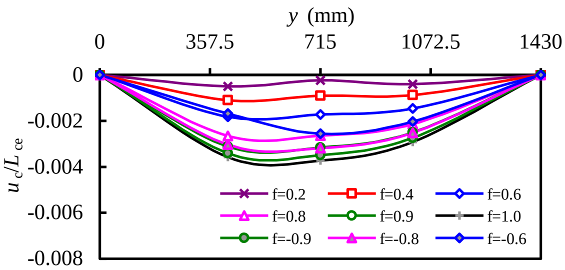

(b) C0.5-0.3-0.2

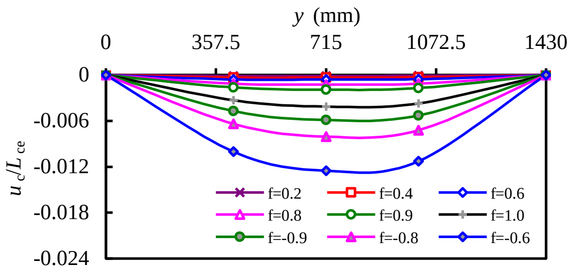

(c) S-0.3-0.2

Fig. 8. Typical distribution pattern of vertical displacements along the span of the chord

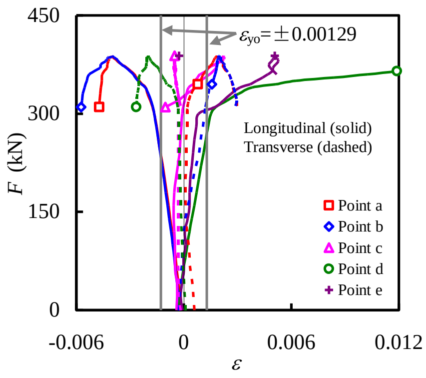

(a) C0.5-0.5-0.2

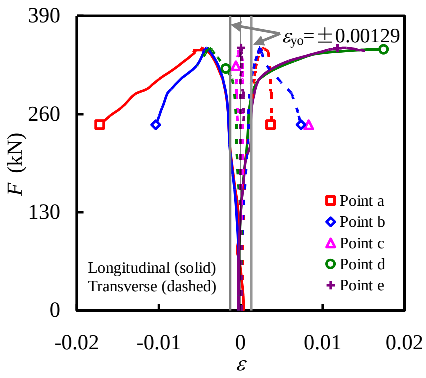

(b) C-0.5-0.2

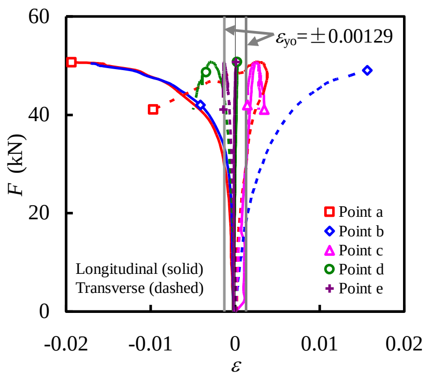

(c) S-0.5-0.2

Fig. 9. F-ε relationship in the chord of typical specimens

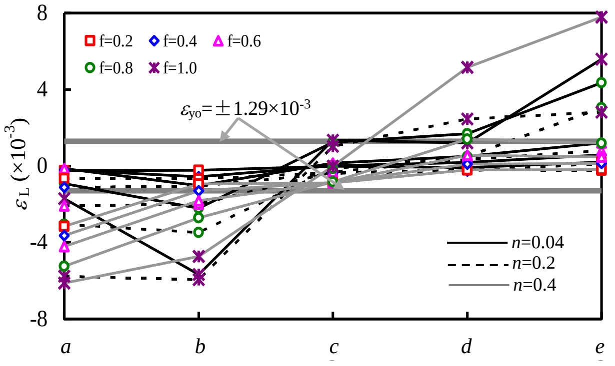

(a) CFDST chord (χ=0.3, β=0.5)

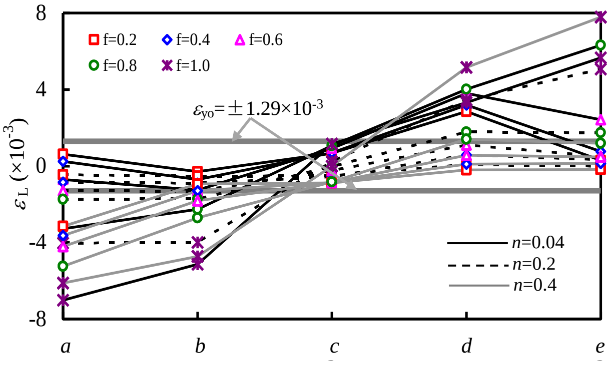

(b) CFDST chord (χ=0.5, β=0.5)

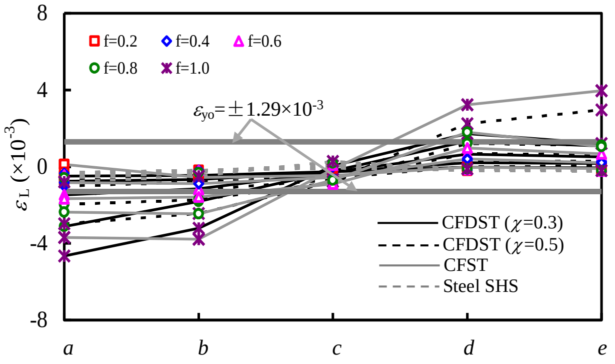

(c) Varied chords (β=0.3, n=0.2)

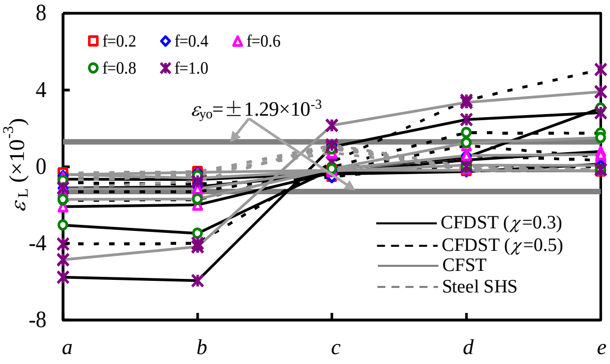

(d) Varied chords (β=0.5, n=0.2)

Fig. 10. Longitudinal strain (ε_L) distribution of the chords under different force ratio (f)

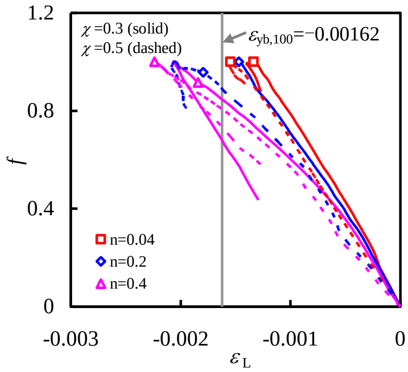

(a) CFDST chord (β=0.5)

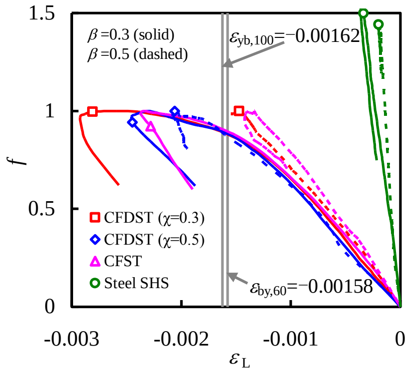

(b) Varied chords (n=0.2)

Fig. 11. Impact of parameters on f-ε_L curves of the steel SHS brace

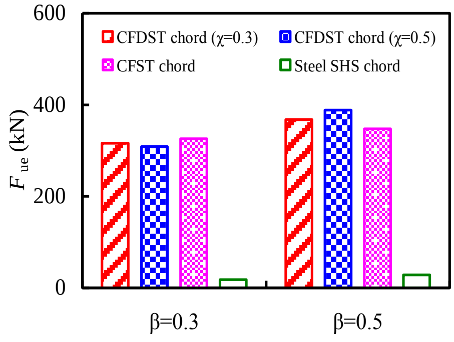

(a) Variation of chord type and β (n=0.2)

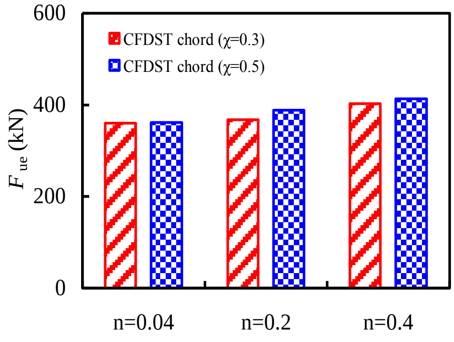

(b) Variation of χ and n (β=0.5)

Fig. 12. Effect of parameters on F_{ue}

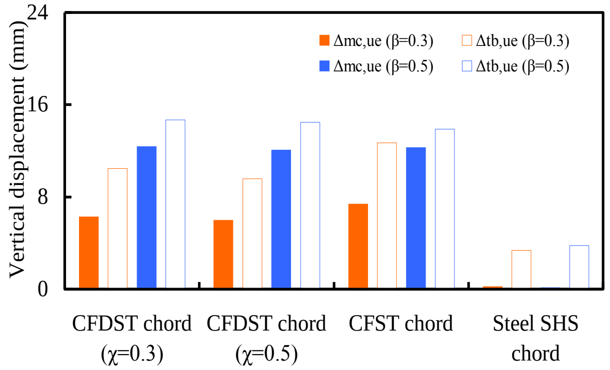

(a) Variation of chord type and β (n=0.2)

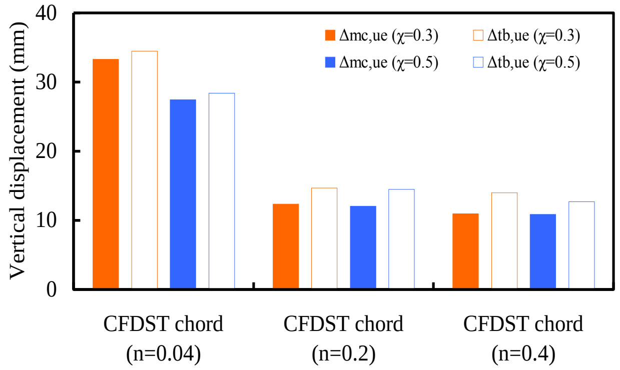

(b) Variation of χ and n (β=0.5)

Fig. 13. Change of $\Delta_{mc,ue}$ and $\Delta_{tb,ue}$

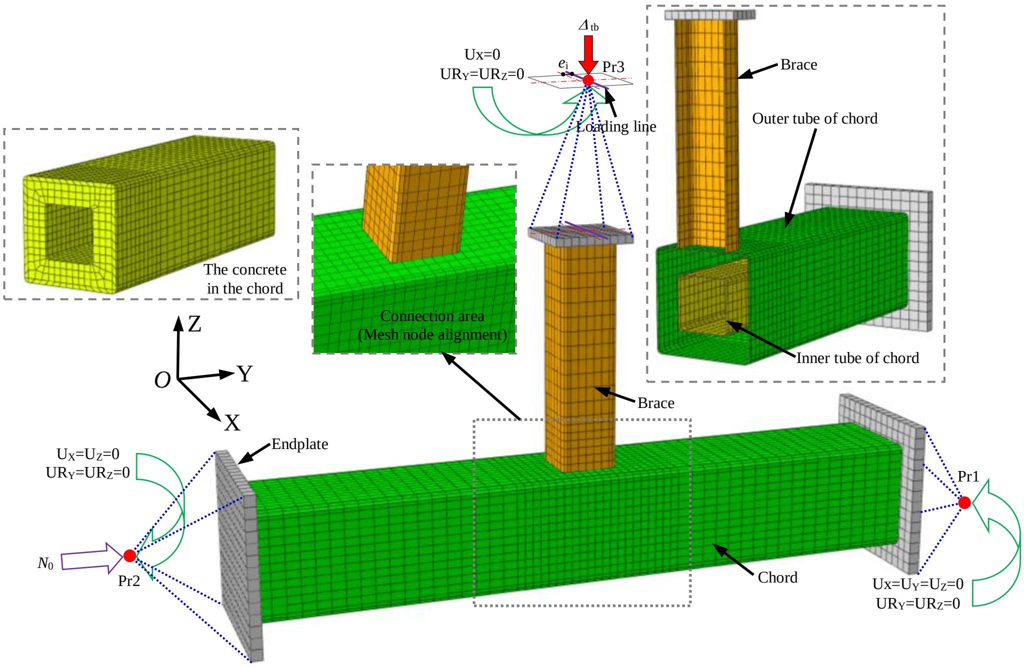

Fig. 14. The FE model with meshing and boundary conditions

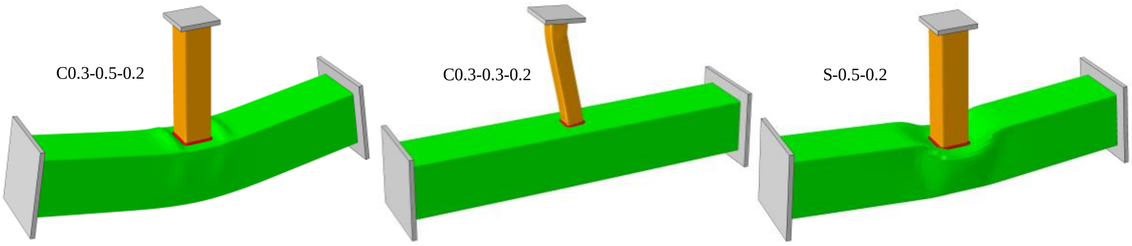

(1) Results with welds

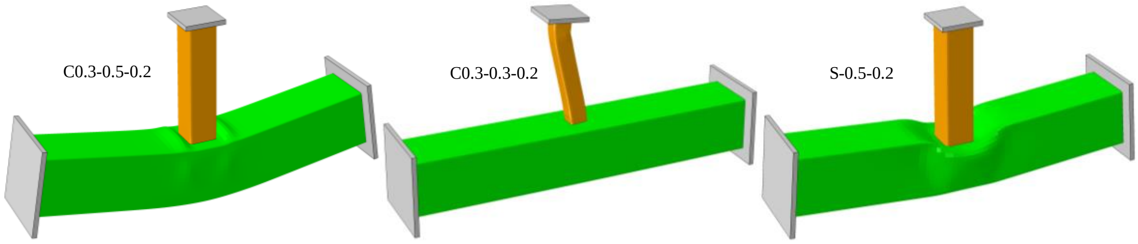

(2) Results without welds

(a) Failure pattern

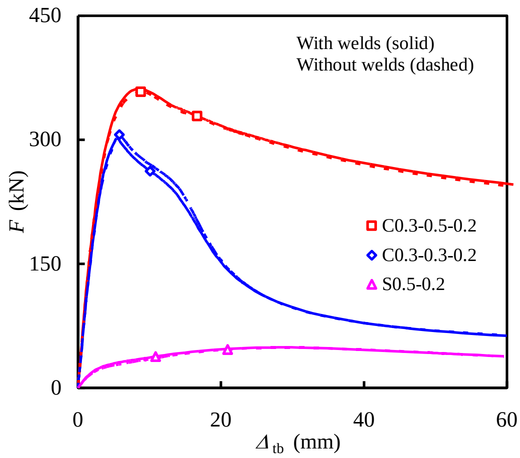

(b) F-Δ_{tb} curves

Fig. 15. Comparison of FE simulation results of the T-joint specimens with and without welds

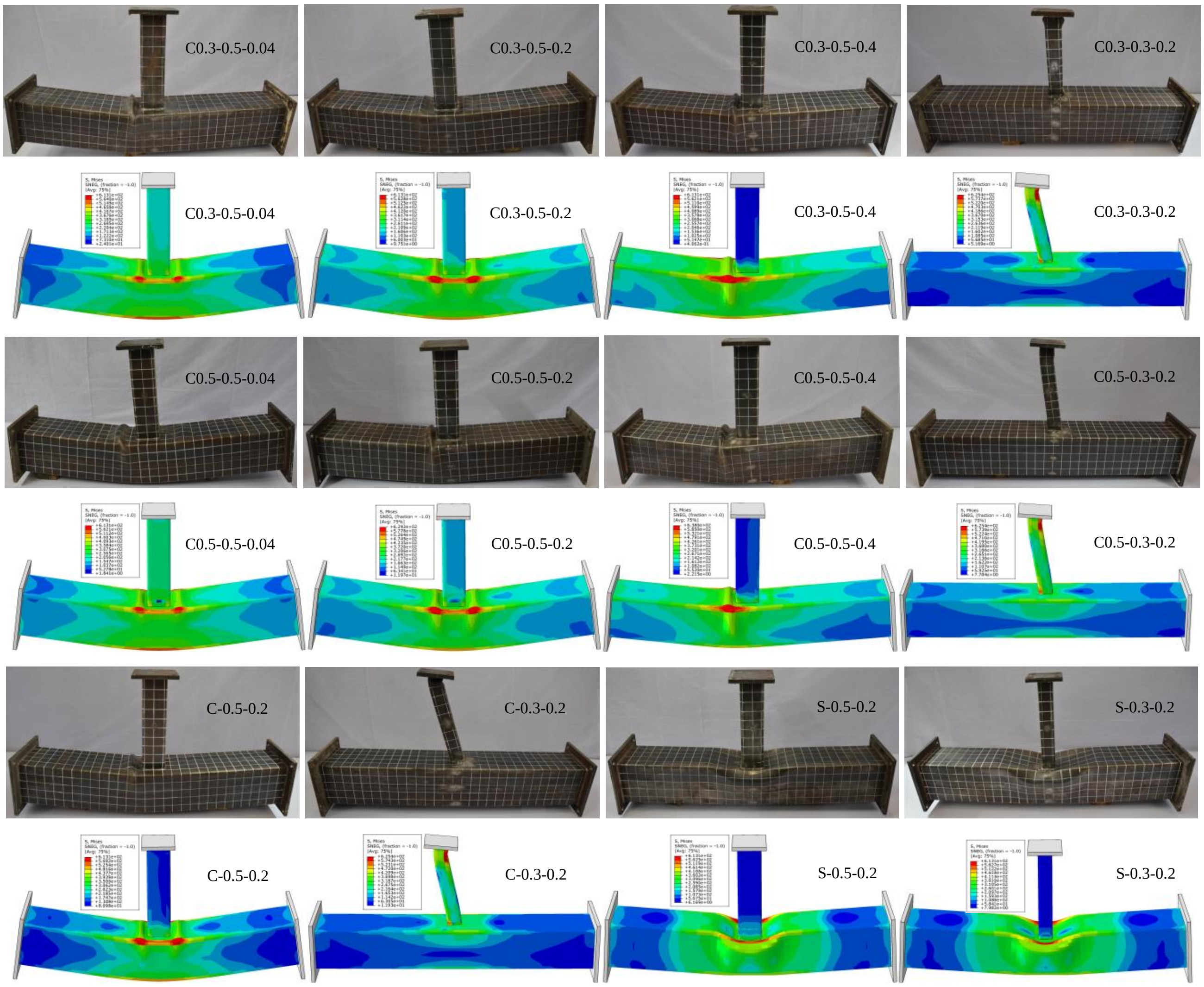

(a) Overall pattern

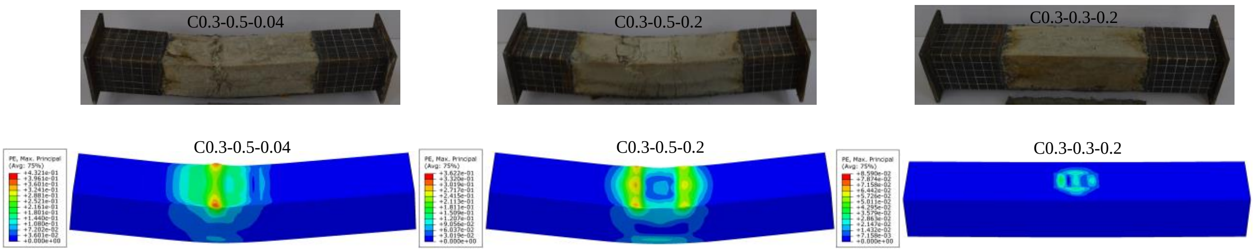

(b) The concrete in the composite chord

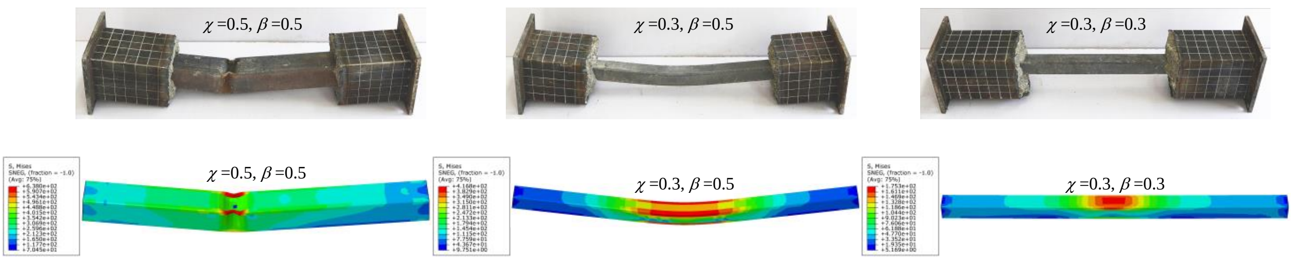

(c) Inner tube of the CFDST chord

Fig. 16. Comparison between the simulated and measured failure patterns

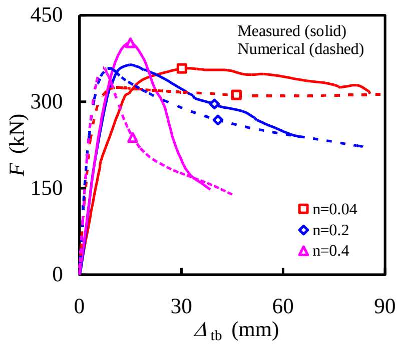

(a) CFDST chord (χ=0.3, β=0.5)

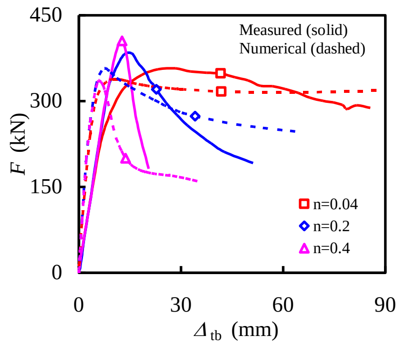

(b) CFDST chord (χ=0.5, β=0.5)

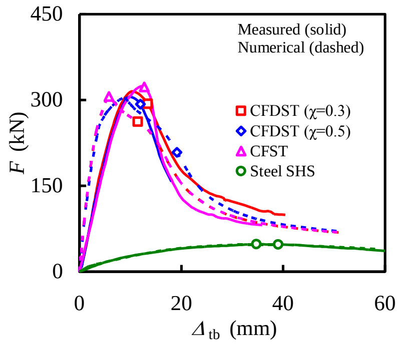

(c) Varied chords (β=0.3, n=0.2)

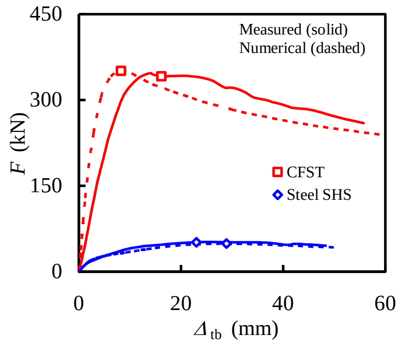

(d) Varied chords (β=0.5, n=0.2)

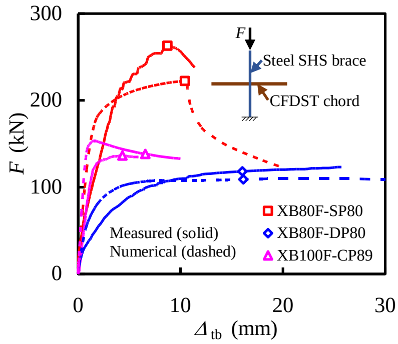

(e) Composite X-joint[11]

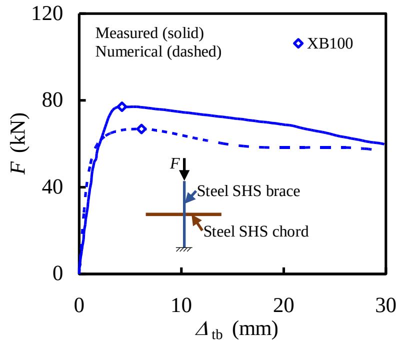

(f) Steel X-joint[11]

Fig. 17. Contrast between the numerical F-Δ_{tb} curves and the measured results

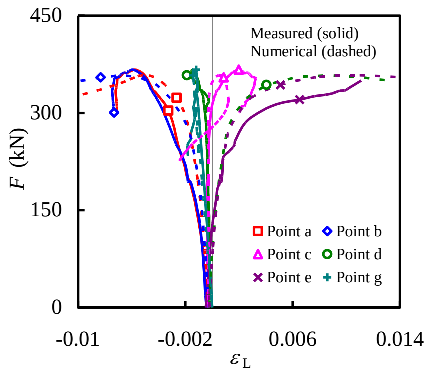

(a) ε_L of C0.3-0.5-0.2

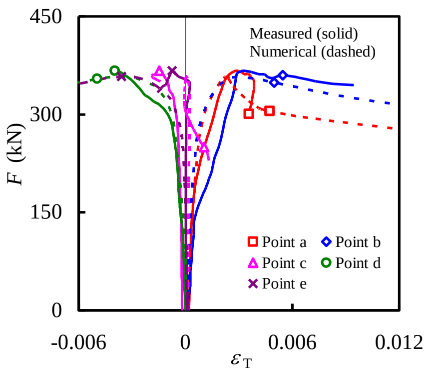

(b) ε_T of C0.3-0.5-0.2

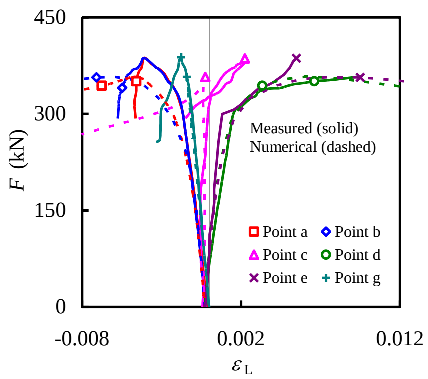

(c) ε_L of C0.5-0.5-0.2

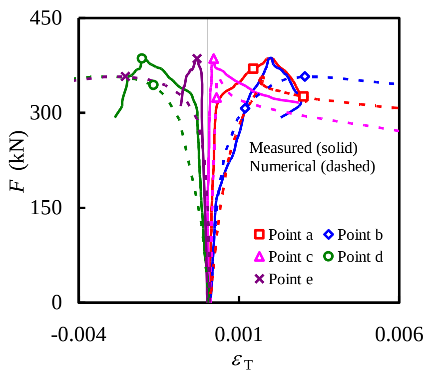

(d) ε_T of C0.5-0.5-0.2

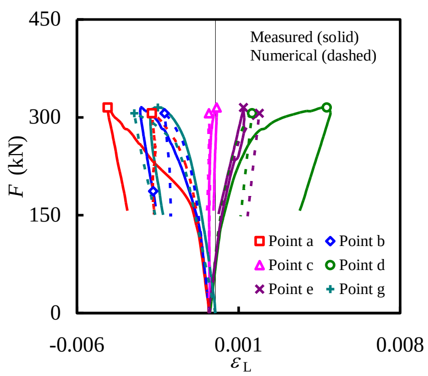

(e) ε_L of C0.3-0.3-0.2

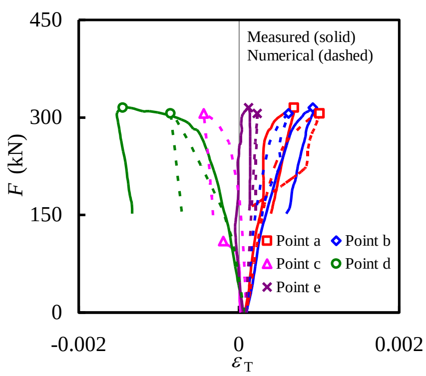

(f) ε_T of C0.3-0.3-0.2

Fig. 18. Typical contrast between the numerical and measured F-$\varepsilon_L(\varepsilon_T)$ relationship

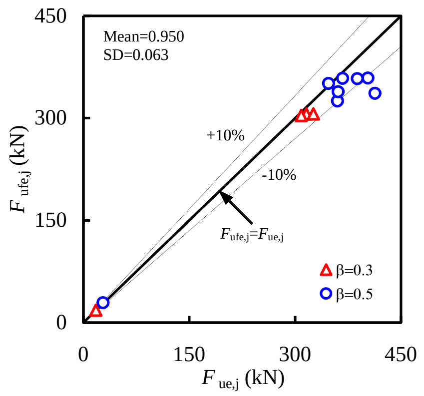

Fig. 19. Contrast between $F_{ufe,j}$ and $F_{ue,j}$

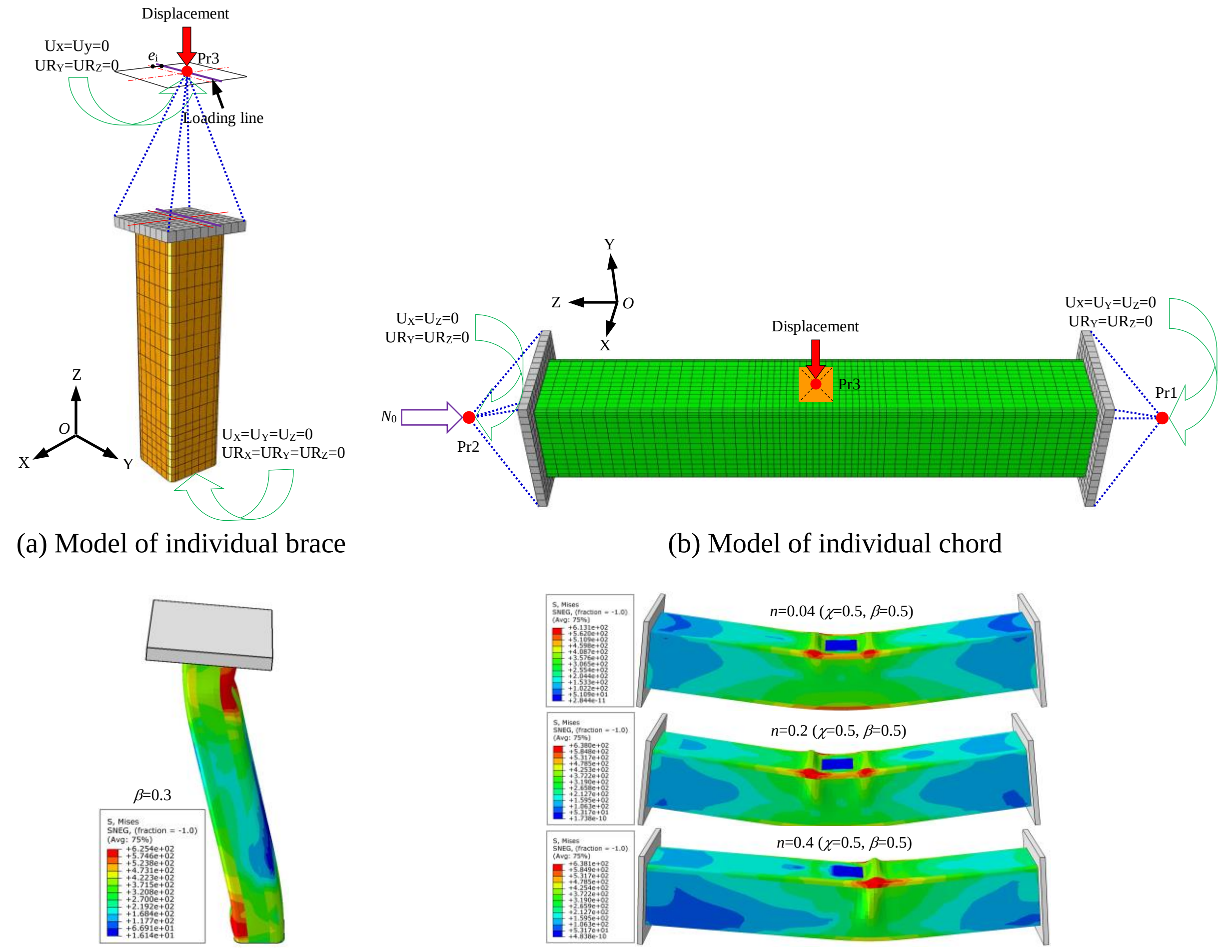

(a) Model of individual brace

(b) Model of individual chord

(c) Failure pattern of individual brace

(d) Failure pattern of individual chord

Fig. 20. FE modelling of the individual components of the composite T-joints

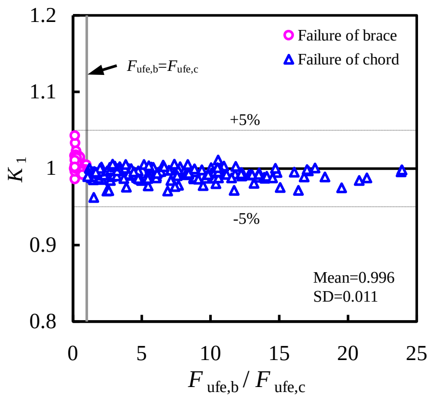

Fig. 21. Variation of K_1 with $F_{ufe,b}/F_{ufe,c}$ values

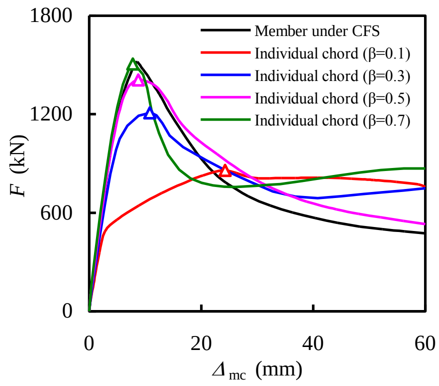

(a) F-Δ_{mc} curves

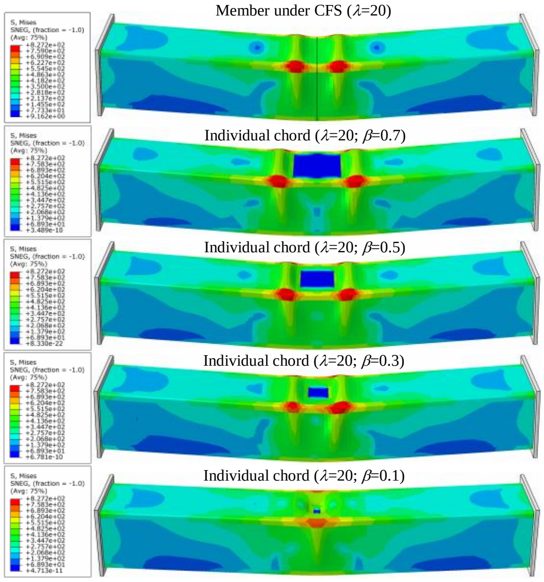

(b) Failure pattern

Fig. 22. Comparison of square CFDST members under different loading conditions

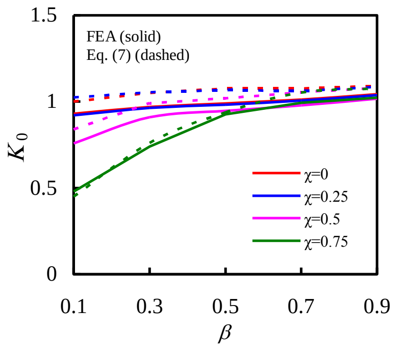

(a) Variation of β and χ

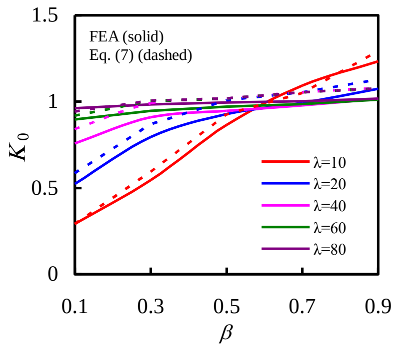

(b) Variation of β and λ

Fig. 23. Effect of typical parameters on K_0

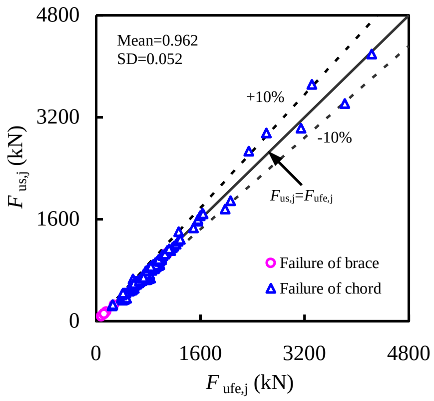

Fig. 24. Contrast between $F_{us,j}$ and $F_{ufe,j}$

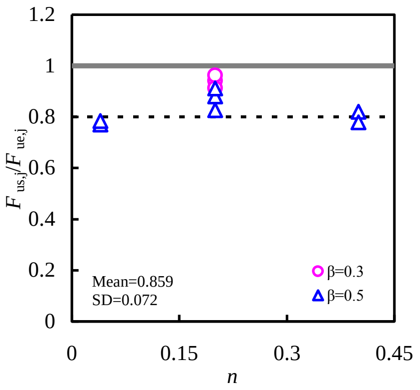

Fig. 25. Variation of $F_{us,j}/F_{ue,j}$ with n and β

Tables:

Table 1 Properties of steel

Type	Width (mm)	Thickness (mm)	Yield strength (MPa)	Tensile strength (MPa)	Modulus of elasticity (N/mm^2)	Poisson's ratio	Elongation after fracture (%)
Chord tube	60	2.94	290.9	355.7	1.85×10^5	0.318	16.9
	100	3.01	299.3	399.7	1.89×10^5	0.292	17.2
	200	4.00	256.0	408.7	1.99×10^5	0.343	33.5
Brace tube	60	4.00	298.2	390.1	1.89×10^5	0.315	14.8
	100	3.85	294.0	377.6	1.81×10^5	0.266	17.1

Table 2 Information of the specimens

No.	Label	Chord		Brace	β	χ	n	N_0 (kN)	$F_{ue,j}$ (kN)	$\Delta_{mc,ue}$ (mm)	$\Delta_{tb,ue}$ (mm)	$F_{ufe,j}$ (kN)	$F_{ufe,j}/F_{ue,j}$	Failure patterns*	
		$b_o\times t_o$ (mm×mm)	$b_i\times t_i$ (mm×mm)	$b_b\times t_b$ (mm×mm)										Observed	Simulated
1	C0.3-0.5-0.04	200×4.00	60×2.94	100×3.85	0.5	0.3	0.04	132.5	360.2	33.3	34.5	325.1	0.902	B+D+F	B+D+F
2	C0.3-0.5-0.2	200×4.00	60×2.94	100×3.85	0.5	0.3	0.2	662.5	367.4	12.4	14.7	358.1	0.975	B+D+F	B+D+F
3	C0.3-0.5-0.4	200×4.00	60×2.94	100×3.85	0.5	0.3	0.4	1325.0	403.1	11.0	14.0	358.9	0.890	B+D+F	B+D+F
4	C0.3-0.3-0.2	200×4.00	60×2.94	60×4.00	0.3	0.3	0.2	662.5	316.0	6.3	10.5	306.3	0.969	A	A
5	C0.5-0.5-0.04	200×4.00	100×3.01	100×3.85	0.5	0.5	0.04	122.9	361.3	27.5	28.4	338.6	0.937	B+D+E	B+D+E
6	C0.5-0.5-0.2	200×4.00	100×3.01	100×3.85	0.5	0.5	0.2	614.5	388.2	12.1	14.5	357.6	0.921	B+D+E	B+D+E
7	C0.5-0.5-0.4	200×4.00	100×3.01	100×3.85	0.5	0.5	0.4	1229.0	413.2	10.9	12.7	336.4	0.814	B+D+E	B+D+E
8	C0.5-0.3-0.2	200×4.00	100×3.01	60×4.00	0.3	0.5	0.2	614.5	308.8	6.0	9.6	304.0	0.984	A	A
9	C-0.5-0.2	200×4.00	--	100×3.85	0.5	/	0.2	661.1	347.6	12.3	13.9	350.8	1.009	B+D	B+D
10	C-0.3-0.2	200×4.00	--	60×4.00	0.3	/	0.2	661.1	325.7	7.4	12.7	306.4	0.941	A	A
11	S-0.5-0.2	200×4.00	--	100×3.85	0.5	/	0.2	169.3	28.1	0.14	3.81	28.9	1.028	C	C
12	S-0.3-0.2	200×4.00	--	60×4.00	0.3	/	0.2	169.3	17.8	0.25	3.38	18.4	1.032	C	C

*: 'A' stands for local buckling of brace, 'B' stands for local buckling of top flange and webs of outer tube in the composite chord, 'C' stands for yielding of top flange and buckling of webs of steel SHS chord, 'D' stands for compressive crushing and tensile cracking of concrete, 'E' stands for local buckling and overall deflection of inner tube in the composite chord, and 'F' stands for overall deflection of inner tube in the composite chord.

Table 3 Contrast of bearing capacity of composite T-joint specimens

No.	Label	$F_{ue,j}$ (kN)	$F_{ufe,j}$ (kN)	$F_{ufe,b}$ (kN)	$F_{ufe,c}$ (kN)	$F_{ufe,bc}$ (kN)	$F_{ufe,j}/F_{ue,j}$	$F_{ufe,bc}/F_{ue,j}$
1	C0.3-0.5-0.04	360.2	325.1	485.3	330.2	330.2	0.902	0.917
2	C0.3-0.5-0.2	367.4	358.1	485.3	361.7	361.7	0.975	0.984
3	C0.3-0.5-0.4	403.1	358.9	485.3	363.9	363.9	0.890	0.903
4	C0.3-0.3-0.2	316.0	306.3	307.3	348.0	307.3	0.969	0.972
5	C0.5-0.5-0.04	361.3	338.6	485.3	342.2	342.2	0.937	0.947
6	C0.5-0.5-0.2	388.2	357.6	485.3	362.6	362.6	0.921	0.934
7	C0.5-0.5-0.4	413.2	336.4	485.3	343.8	343.8	0.814	0.832
8	C0.5-0.3-0.2	308.8	304.0	307.3	313.7	307.3	0.984	0.995
9	C0-0.5-0.2	347.6	350.8	485.3	356.2	356.2	1.009	1.025
10	C0-0.3-0.2	325.7	306.4	307.3	343.0	307.3	0.941	0.944
					Mean		0.934	0.945
					SD		0.056	0.054